

# Multi-Image Optimization based Specular Reflection Removal from Non-dielectric Surfaces

J. W. Bonekamp

Master of Science Thesis



# **Multi-Image Optimization based Specular Reflection Removal from Non-dielectric Surfaces**

MASTER OF SCIENCE THESIS

For the degree of Master of Science in Systems and Control at Delft  
University of Technology

J. W. Bonekamp

August 12, 2021

Faculty of Mechanical, Maritime and Materials Engineering (3mE) · Delft University of  
Technology



Copyright © Delft Center for Systems and Control (DCSC)  
All rights reserved.



DELFT UNIVERSITY OF TECHNOLOGY  
DEPARTMENT OF  
DELFT CENTER FOR SYSTEMS AND CONTROL (DCSC)

The undersigned hereby certify that they have read and recommend to the Faculty of  
Mechanical, Maritime and Materials Engineering (3mE) for acceptance a thesis  
entitled

MULTI-IMAGE OPTIMIZATION BASED SPECULAR REFLECTION REMOVAL FROM  
NON-DIELECTRIC SURFACES

by

J. W. BONEKAMP

in partial fulfillment of the requirements for the degree of  
MASTER OF SCIENCE SYSTEMS AND CONTROL

Dated: August 12, 2021

Supervisor(s):

\_\_\_\_\_  
prof.dr.ir. M. Verhaegen

\_\_\_\_\_  
Dr.ir. O. Soloviev

\_\_\_\_\_  
ir. J. Noom

Reader(s):

\_\_\_\_\_  
dr.ir. R. van de Plas



---

# Abstract

Specular light reflections are the mirror-like reflections from a material interface. They appear in the observation of any illuminated surface. Specular reflections can be set apart from the diffuse reflection type, which has a random distribution of reflection directions. The radiance of the specular reflected light is governed by the *Fresnel ratio* and depends on both geometrical and spectral properties. A clear distinction can be made between the reflection properties of dielectric and the much more reflective non-dielectric material types. In certain cases the presence of specular reflections is useful, for example in object identification or computer graphics applications. However, often the presence of specular reflection causes bright spots on the image of an object, which results in loss of detail in these areas. Particularly in computer vision applications it is important to only observe the intrinsic diffuse reflection. Hence, a variety of specular reflection removal methods have been developed.

Color-space analysis specular reflection removal methods are able to accurately recover the intrinsic diffuse color of the image of an object. Optimization based methods based on a non-negative matrix factorization of the data are considered. The reduced characteristic representation of the data allows the specular and diffuse reflection component to be separated more easily. A multi-image approach is considered because it provides more available information on the intrinsic diffuse reflection component, which is typically a relatively weak signal for non-dielectric surface reflections.

A specular reflection removal method is developed, that combines a new reflection model for colored illumination with a sparse Non-negative Matrix Factorization (NMF) optimization in a multi-image framework. The proposed method is evaluated on synthetic data and real data images of non-dielectric materials acquired conform the proposed reflection model.



---

# Table of Contents

<b>Preface</b>	<b>ix</b>
<b>1 Introduction</b>	<b>1</b>
1-1 Specular reflection highlights . . . . .	1
1-2 Surface reflection of light . . . . .	2
1-3 Thesis motivation . . . . .	7
1-4 Outline . . . . .	7
<b>2 Specular Reflection Removal Methods</b>	<b>9</b>
2-1 Specular reflection removal methods . . . . .	9
2-1-1 Single-image specular reflection removal methods . . . . .	9
2-1-2 Multi-image specular reflection removal methods . . . . .	12
2-2 Non-negative matrix factorization . . . . .	13
2-2-1 Non-negative matrix factorization . . . . .	13
2-2-2 Akashi and Okatani's specular reflection removal method . . . . .	14
<b>3 Multi-image optimization based specular reflection removal for non-dielectric objects</b>	<b>19</b>
3-1 Surface reflection model . . . . .	19
3-2 Multi-image optimization based specular reflection removal for non-dielectric objects	21
<b>4 Results and discussion</b>	<b>25</b>
4-1 Experiment description . . . . .	25
4-1-1 Data acquisition . . . . .	25
4-1-2 Evaluation method . . . . .	28
4-2 Experimental results . . . . .	28
4-2-1 Results for synthetic data sets . . . . .	29
4-2-2 Results for non-dielectric data sets . . . . .	32
4-3 Discussion . . . . .	37

<b>5 Conclusion</b>	<b>39</b>
5-1 Summary of study . . . . .	39
5-2 Outlook . . . . .	40
<b>Bibliography</b>	<b>43</b>
<b>Glossary</b>	<b>47</b>
List of Acronyms . . . . .	47
List of Symbols . . . . .	47

---

# List of Figures

1-1	Left: Specular highlights observed as bright spots on a dielectric object. (source: [30]). Right: Specular highlights on a aluminum- and manganese, non-dielectric objects. The specular highlights appearing on non-dielectric objects tend to be more bright and larger in size. . . . .	2
1-2	Schematic drawing of the interface reflection geometry in the plane of incidence, which is defined by the direction of the illumination source, $I$ , and the direction of the surface normal, $N$ . The direction of the macroscopic perfect specular reflection is given by, $R$ . The vector, $T$ , denotes the direction of the transmitted light. The angles between the different directions and the surface normal are given by $\theta_i$ , $\theta_r$ and $\theta_t$ . . . . .	3
1-3	Schematic drawing of possible reflection directions for the incident light at macroscale. In red the distribution of the possible directions for the diffuse component. In blue the distribution of the possible directions of the specular reflections. The illumination direction is given by $I$ . While $L$ and $R$ , denote the direction to a viewpoint and the macroscopic perfect specular reflection direction, respectively. The angles between the directions are given by $\theta_g$ , $\theta_s$ and $\theta_e$ . . . . .	5
1-4	Schematic representation of the Dichromatic Reflection Model (DRM). The incident light is either specularly reflected or diffusely reflected after scattering by particles within the material. (Figure after [27]) . . . . .	6
2-1	Pixel clustering in RGB color space of pixels from an image with a single diffuse color and a specular highlight. The pixels lie on the same plane spanned by the diffuse color direction, $\mathbf{i}_d$ , and specular color direction, $\mathbf{i}_s$ . (Figure after [15]) . . .	10
2-2	Results for the method in [1] for both a dielectric and non-dielectric object. The input image on the left is separated into a specular and diffuse image. Individual images are scaled for maximum contrast. . . . .	16
4-1	Overview of the experimental setup for acquiring data images of non-dielectric objects. A non-dielectric sample is illuminated by a (color-filtered) LED-array illumination. The images are captured by a scientific camera positioned in the direction of the sample surface normal. Note that for acquisition of the actual data sets the room illumination is switched off and the camera/illumination source positions are different. . . . .	26

4-2	Set of images of the color-filtered LED-array illumination source used within the experiment. The corresponding normalized average RGB-color and relative average intensity with respect to the white illumination source are shown. These colors are used within the implementation as the known normalized specular color vectors. .	27
4-3	Overview of the generated synthetic data set. The true diffuse image (top-right) is assumed to be uniformly illuminated with different illumination colors equal to the specular colors, which gives the projected diffuse images. The projected diffuse images summed with the specular images gives the data images, which can be used as input within the implementation. Note that the intensity of individual images is scaled for maximum contrast. . . . .	27
4-4	Results for synthetic data set as input, with three input images and $R = 3$ , $\rho_s = 1$ and $\rho_d = 3$ . The intensity of individual images is scaled for contrast. . . . .	29
4-5	Double logarithmic convergence results for the synthetic data set with 3 input images. The total cost function value $J_2$ from Eq. (3-6) shows a decreasing behaviour and the convergence criteria is reached after 4280 iterations in 1561 seconds. . .	30
4-6	Results for synthetic data set as input, with five input images and $R = 3$ , $\rho_s = 1$ and $\rho_d = 3$ . The intensity of individual images is scaled for contrast. . . . .	31
4-7	Recovered diffuse image ( $W_d H_d$ ) for different combinations of the specular- and diffuse regularization parameters, ( $\rho_s$ , $\rho_d$ ). Additionally, the Structural Similarity Index (SSIM), Mean Squared Error (MSE) and average column sparsity of $H_d$ are given. . . . .	32
4-8	Acquired data images of a non-dielectric aluminum plate with profile. Both the original images and gamma corrected ( $\gamma = 2$ ) data is shown. Multiple specular highlights appear on the edges of the profile and one larger specular highlight is present on the main surface. The location of specular highlights are indicated in the green sub-image. The images are scaled for maximum contrast. . . . .	33
4-9	Results for input data images of a non-dielectric aluminum profile plate, with parameters set to $R = 1$ , $\rho_s = 2$ and $\rho_d = 1$ . The data is reconstructed through the summation of a specular image and projected diffuse image estimate. The specular estimate image indicates a correct localization of the specular highlights in the data. . . . .	34
4-10	Left: Reconstructed diffuse image ( $W_d H_d$ ) of the non-dielectric aluminum profile, corresponding to the results in Figure 4-9. The image is gamma corrected ( $\gamma = 2$ ) and scaled for maximum contrast. Right: Double logarithmic convergence results for the data set of a non-dielectric profile plate. The convergence criteria is reached after 294 iterations in 598 seconds. . . . .	34
4-11	Acquired data images of a non-dielectric messing object. Both the original data images and gamma corrected ( $\gamma = 2$ ) data are shown and scaled for maximum contrast. A large single specular highlight can be distinguished on each of the sub-images, together with a weaker specular highlight where the surface normal of the object is in the direction of the camera. . . . .	35
4-12	Results for input data images of a non-dielectric messing object, with parameters set to $R = 2$ , $\rho_s = 5$ and $\rho_d = 2$ . The data is reconstructed through the summation of a specular- and projected diffuse image estimate. The images are with gamma correction ( $\gamma = 2$ ) and scaled for maximum contrast. . . . .	36
4-13	Left: Reconstructed diffuse image ( $W_d H_d$ ) of the non-dielectric messing object, corresponding to the results in Figure 4-12, image is with gamma correction ( $\gamma = 2$ ) and scaled for maximum contrast. The dashed red line indicates the pixels for which the specular- and diffuse coefficients are given in Figure 4-14. Right: Double logarithmic convergence results for the data set of a non-dielectric profile plate. The convergence criteria is reached after 205 iterations in 403 seconds. . . . .	36

- 
- 4-14 The reconstructed specular coefficients (from  $H_s$ ) and object color diffuse coefficients (from  $H_d$ ) for the pixels indicated by the dashed line on the left image in Figure 4-13 located at the specular highlight. . . . . 37



---

# Preface

This document contains the results of a thesis project on specular reflection removal from non-dielectric surfaces. The purpose of this study is to investigate whether an optimization based specular reflection removal method for non-dielectrics objects can be developed. The thesis will be the final step in completing the Master's degree in Systems and Control at the Delft University of Technology. The project is carried out at the Delft Center for Systems and Control (DCSC), within the Numerics for Control and Identification (N4CI) group under supervision of prof.dr.ir. M. Verhaegen together with daily supervisors dr.ir. O.A. Soloviev and ir. J. Noom.

Special thanks go out to Jacques. Our weekly (digital) meetings and discussions made me look critically at my work. This really helped me in putting together the surface reflection model. I also want to mention the regularly scheduled student seminars within our group organized by Oleg. Presenting my progress and listening to the projects of other students, always agitated my enthusiasm for this thesis and scientific research in general.



“For light I go directly to the source of light, not to any of the reflections.”

– *Mildred Norman*



---

# Chapter 1

---

## Introduction

Specular reflection highlights appear in many photographed images and are part of the realistic presentation of an imaged scene. However, the highlights can also obscure information of the objects in the scene, which is why in certain applications we require ways to remove the specular highlights. In this chapter we first describe in Section 1-1 the general concept of specular highlights together with the relevance they have in certain applications. In Section 1-2 the most important concepts affecting the formation of specular- and diffuse reflection components are introduced. The motivation and outline for this thesis is given in Section 1-3 and Section 1-4, respectively.

### 1-1 Specular reflection highlights

Specular reflections are the mirror-like reflections of light that theoretically are present on any illuminated surface. The main relation governing this phenomenon is the *law of reflection*, which states that the angle of the incident light direction is equal to the angle of the reflected light direction. Specular light reflections typically present themselves as white bright spots (i.e. specular highlights) to an observer. Figure 1-1 shows such a typical occurrence of specular reflections on the image of a selection of illuminated objects.

The presence of specular reflections can assist an observer in the depth perception of an object. Moreover, the specular reflection is an indication of the surface texture and material type. However, at the bright specular highlights itself there is a loss of detail, because the underlying color or texture of the object can become harder to distinguish. In contrast with specular reflection, the diffuse reflection from a surface is not governed by the law of reflection and is generally assumed to be an intrinsic property of the object. In literature there has been confusion about the naming convention of reflections. Throughout this study light reflections obeying the law of reflection will be referred to as *specular reflections* and all other types of light reflections will be called *diffuse reflections*.

The phenomenon of specular reflection has been used in a wide range of applications. For example in both [5] and [33] the presence of specular reflection and geometrical models are use

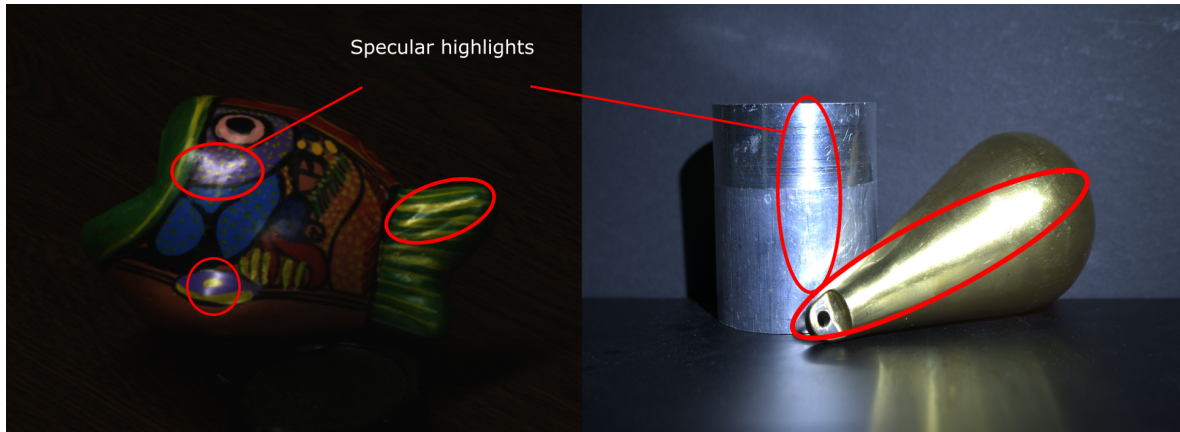


**Figure 1-1:** Left: Specular highlights observed as bright spots on a dielectric object. (source: [30]). Right: Specular highlights on a aluminum- and manganese, non-dielectric objects. The specular highlights appearing on non-dielectric objects tend to be more bright and larger in size.

to identify the geometry of an observed object and in [7] the difference in specular reflections are used to characterize certain carbon-filled polymers. In computer graphics, models of specular reflections are used to generate realistic scenes, pioneering work has been done in [24]. However, many applications in the field of photography and computer vision require images with minimal specular reflections. For example the automated road detection algorithm in [28], where a specular reflection removal method is used to improve the performance. Also in many computer vision applications that use some form of automated material identification or defect inspection, the specular highlights can affect the performance significantly.

## 1-2 Surface reflection of light

In the literature study on specular reflections performed in preparation for this thesis, the physical phenomenon and mathematical relations governing the reflection of light at the interface of two media was investigated [34]. In this section the most important notions are summarized for reference.

Light is a transverse electromagnetic wave with a certain wavelength, denoted by  $\lambda$ . A light-ray with a certain wavelength can either be reflected or transmitted at the interface of two media. The direction in which the light is reflected is governed by the *law of reflection*. This states that the reflection angle with respect to the surface normal,  $\theta_r$ , is equal to the angle of incident light with respect to the surface normal,  $\theta_i$ . A schematic overview of surface reflection at an interface of two media is given in Figure 1-2. Typically, the first medium is air and the second medium is an arbitrary material.

The fraction of incident light that is specular reflected is determined through the Fresnel equations [9]. This implies the portion of specular reflected light, or the *Fresnel ratio* denoted by  $R$ , is a function of a number of variables:

$$R = f(\text{wavelength, geometry, material, polarization}). \quad (1-1)$$

In the context of this thesis the following notions about the variables in Eq. (1-1) are important to grasp:

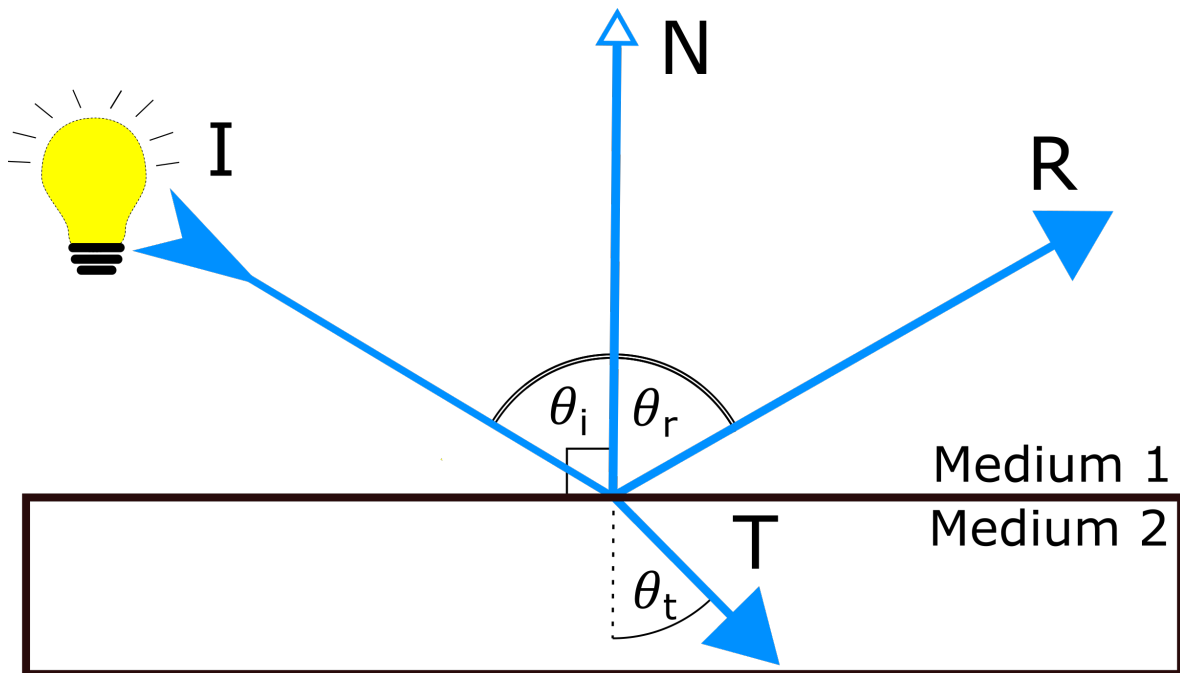


**Figure 1-2:** Schematic drawing of the interface reflection geometry in the plane of incidence, which is defined by the direction of the illumination source,  $I$ , and the direction of the surface normal,  $N$ . The direction of the macroscopic perfect specular reflection is given by,  $R$ . The vector,  $T$ , denotes the direction of the transmitted light. The angles between the different directions and the surface normal are given by  $\theta_i$ ,  $\theta_r$  and  $\theta_t$ .

- The Fresnel ratio can vary for different wavelengths of the incident light. Typically this variation is small, which makes it a fair assumption that the Fresnel ratio is equal for all wavelengths, and therefore the specular color spectrum is the same as the illumination color spectrum. However for some materials this is not necessarily the case.
- The magnitude of the Fresnel ratio strongly depends on the incident angle of light. Especially at grazing angles ( $\theta_i$  approaching 90 degrees) the ratio can sharply increase, up to complete specular reflection. The dependency on the geometry can also deviate for different wavelengths of the incident light. Typically, the dependency of the Fresnel ratio on both the incident wavelength and incident angle of illumination are less prominent for normal incident light ( $\theta_i$  close to 0 degrees) [4, 23].
- The Fresnel ratio is also a function of the material type, mainly through the magnetic properties of the material. A clear distinction between *dielectric* and *non-dielectric material* types can be made. Dielectrics are non-conducting materials, like glass, polymers and ceramics. Typically, the Fresnel ratio for dielectric materials is approximately the same over the visible range of wavelengths (380 to 750 nm). It is therefore a fair assumption that the specular reflection of normal incident light is of the same visual color. However, for non-dielectric (conducting) materials this is not always case. The stronger magnetic properties for non-dielectric materials also imply that the typical Fresnel ratio for non-dielectrics are larger values than for dielectric materials, which explains why non-dielectric materials tend to have brighter and larger specular highlights [4, 23].

- Polarization refers to the orientation of the electromagnetic field of light with respect to the plane of incidence. The overall Fresnel ratio,  $R$ , is actually a weighted sum of the Fresnel reflection ratio's for the component of incident light with an electric field perpendicular- and parallel to the plane of incidence. These individual ratio's can vary strongly dependent on geometry and wavelength, and therefore the specular reflections tend to be polarized light. Again, this effect is stronger for larger incident illumination angles.

However, not all incident light is reflected directly at the interface. In Figure 1-2 we see that a portion of the incident light can be aberrated and transmitted. The transmittance angle,  $\theta_t$ , can be described through Snell's law. And the transmittance ratio is given by:

$$T = 1 - R. \quad (1-2)$$

The definition for the ratio of transmitted light,  $T$ , in Eq. (1-2) indicates that it depends on the same variables as the Fresnel ratio. Note that a number of things can happen to the transmitted light. The transmitted light can be emitted back after scattering within the material. This is referred to as the *diffuse reflection* of a material. But the light can also be absorbed by the material or transmitted out of the material on the backside. For opaque surfaces no light is transmitted out of the material on the backside, thus all light is either absorbed or re-emitted. The re-emitted diffuse type of reflection generally undergoes scattering within the material before being re-emitted. Therefore this type of reflection tends to be unpolarized and the random character of scattering implies a homogeneous distribution of diffuse reflection directions.

Within this thesis it is assumed that the material surfaces are not optically active and do not have any thin-film properties. However, we do consider the impact of surface roughness on the specular reflections. For non-perfectly smooth surfaces, locally the surface normal can deviate from the macroscopic surface normal. In turn the local specular reflection direction can deviate from the macroscopic specular reflection direction. Typically, we can assume a random distribution of the local deviations from the macroscopic surface normal. This implies the specular reflections from a certain illumination direction, have a distribution around the macroscopic specular reflection direction, dependent on the surface roughness of the material. In Figure 1-3 a schematic drawing of the distribution of reflection directions is given for both the diffuse- and specular reflection component. Additionally, an arbitrary observer direction, denoted by  $L$ , is indicated. Often we are confronted with the combination of the diffuse- and specular reflection components in this particular direction.

Indeed light surface reflection models aim to model the radiance and color of light in the observer direction. Early reflection models originate from computer graphics. These models, or *shaders*, typically only determined the reflections of a surface based on the type of material, and the orientation of the surface with respect to the illumination [11]. The *Phong shading model* [24] was one of the first models that distinguished between the diffuse- and specular reflection component with two separate terms.

A more general and widely accepted reflection model is described in [27], where the Dichromatic Reflection Model (DRM) is proposed. This is a model for opaque, optically inactive and inhomogeneous materials. This implies that incident light will only interact with a medium and particles that produce scattering and coloration. Note that this makes the considered

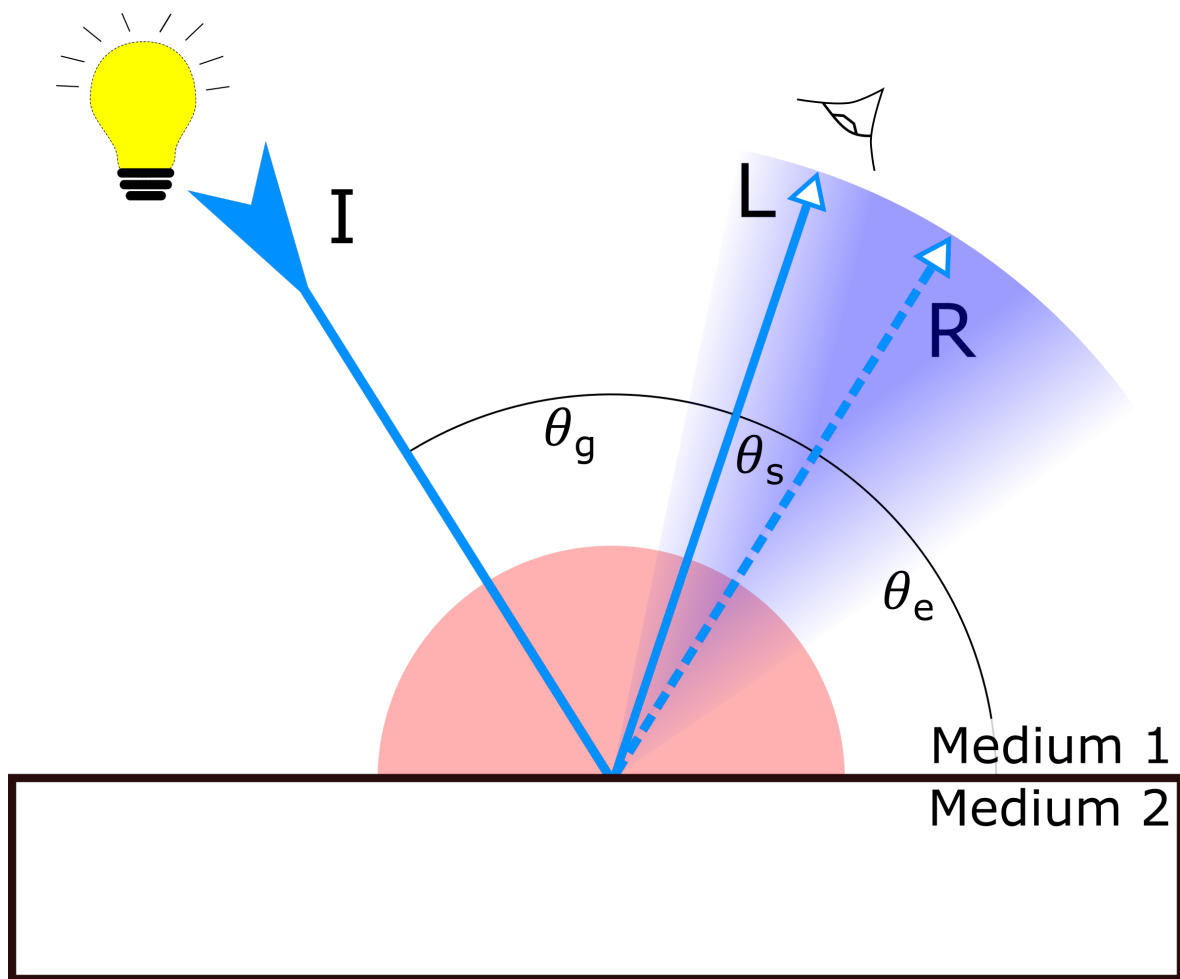


**Figure 1-3:** Schematic drawing of possible reflection directions for the incident light at macroscale. In red the distribution of the possible directions for the diffuse component. In blue the distribution of the possible directions of the specular reflections. The illumination direction is given by  $I$ . While  $L$  and  $R$ , denote the direction to a viewpoint and the macroscopic perfect specular reflection direction, respectively. The angles between the directions are given by  $\theta_g$ ,  $\theta_s$  and  $\theta_e$ .

model less valid for optically homogeneous materials, like metals, at larger incident angles of the illumination.. The main mechanisms of reflection that are modeled in the DRM are illustrated in Figure 1-4. The DRM is a general formulation that takes into account most of the physical phenomenon governing the surface reflection of light. The incident light is either specularly reflected or transmitted, governed by the Fresnel ratio. The direction of specular reflections is determined by the *law of reflection*, however the actual direction may differ from the macroscopic perfect specular direction due to surface roughness. The transmitted light will undergo scattering by the particles within the material. For opaque, non-optically active materials it is assumed that all light will be re-emitted through the same interface it came from after scattering. The re-emitted light will have a diffuse distribution due to the scattering and the color can be changed by the wavelength dependent absorption of the particles. Because the specular reflection is governed by the Fresnel equations, it tends to be polarized

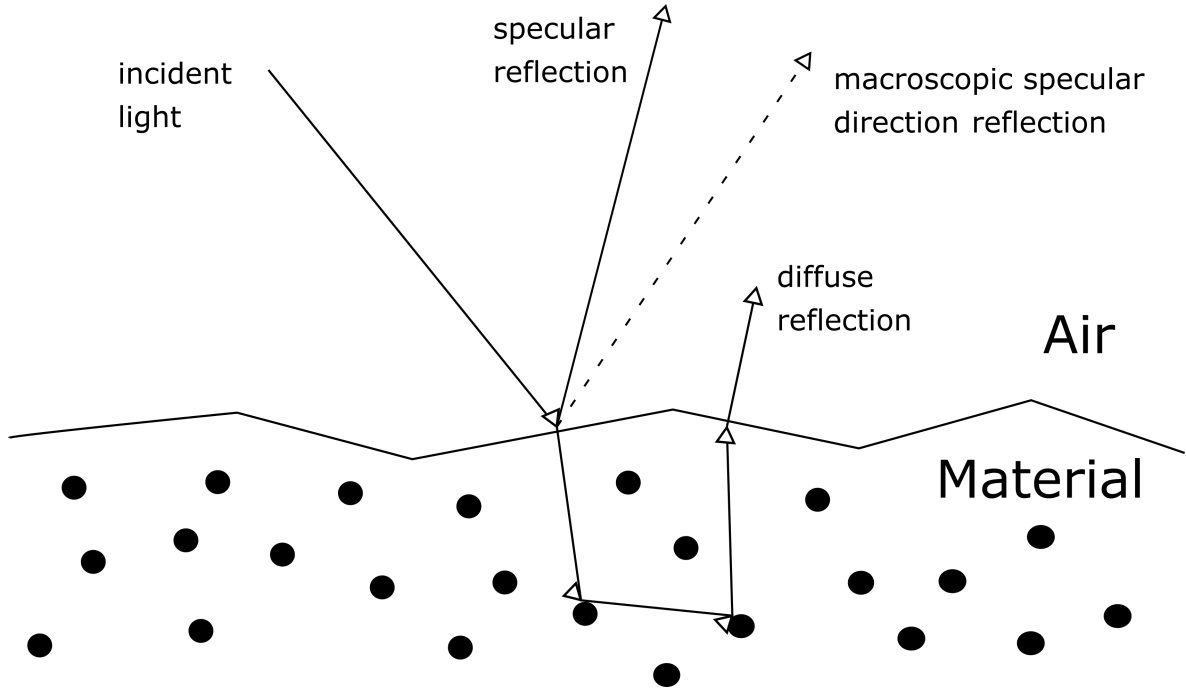


**Figure 1-4:** Schematic representation of the Dichromatic Reflection Model (DRM). The incident light is either specularly reflected or diffusely reflected after scattering by particles within the material. (Figure after [27])

light, while the diffuse reflection is assumed to be unpolarized. The DRM can be described mathematically as in Eq. (1-3).

$$\begin{aligned} L(\lambda, \theta_i, \theta_e, \theta_g) &= L_d(\lambda, \theta_i, \theta_e, \theta_g) + L_s(\lambda, \theta_i, \theta_e, \theta_g) \\ &= m_d(\theta_i, \theta_e, \theta_g)c_d(\lambda) + m_s(\theta_i, \theta_e, \theta_g)c_s(\lambda) \end{aligned} \quad (1-3)$$

Here the total radiance in a viewpoint,  $L$ , is modeled as the sum of independent diffuse and specular radiance terms,  $L_d$  and  $L_s$ , respectively. The geometric dependence of both parts is modeled through the geometric scaling factors,  $m_d$  and  $m_s$ , for the diffuse- and specular part, respectively. The color composition is modeled through relative spectral power distributions,  $c_d(\lambda)$  and  $c_s(\lambda)$ . This separation of the geometric and color composition of both reflections, makes this model applicable to a large range of objects and scenes. Moreover, there are no assumptions on the geometry of the illumination and reflection. However, it does still leave the problem of finding accurate functions for the geometric- and color compositions. Note that especially at larger incident angles it is unrealistic to assume the color composition of reflected light is totally independent from geometry. This applies in particular for non-dielectric materials, because the Fresnel ratio can strongly differ for different wavelengths at larger angles of incidence. The general formulation and decomposition of specular- and diffuse terms in geometry and spectral factors of makes the DRM model suitable for specular reflection removal methods, which will be discussed in Section 2-1.

## 1-3 Thesis motivation

From the previous sections we gather that the presence of specular highlights can be a nuisance for computer vision applications. Especially, non-dielectrics materials have reflection properties, that can generate relatively large and bright specular highlights. Additionally, the modeling of reflection components is more difficult for non-dielectrics, because the decoupling of geometry and spectral factors cannot be generally assumed. In the literature study it has become clear that there does not exist a simple method for acquiring a specular-free image of non-dielectric materials. In fact, it is generally posed that a multi-image approach with a complex imaging setup is required for effective specular reflection removal from non-dielectric materials. However, Chapter 2 will show that there are single-image methods with working principles that under a number of assumptions can be effective for specular reflection removal from non-dielectrics. These working principles are rarely used in existing multi-image specular reflection removal methods. In this thesis a specular reflection removal method is proposed, that combines Non-negative Matrix Factorization (NMF) optimization techniques in a multi-image framework.

## 1-4 Outline

This document has the following structure. In Chapter 2 the advantages and shortcomings of a selection of specular reflection removal methods will be discussed. This motivates the development of a new specular reflection removal method for non-dielectric materials, which is the main contribution of the thesis described in 3. The experiment and results are discussed in Chapter 4. The thesis is then concluded in Chapter 5, with a summary and recommendations on ways to further improve the specular reflection removal from non-dielectric materials.



# Specular Reflection Removal Methods

In this chapter an overview is given of illustrative specular reflection removal methods in literature. We focus on the effectiveness and shortcomings the working principles display with respect to the specular reflection removal from non-dielectric materials. In Section 2-1 a selection of methods are discussed, organised by single-image and multi-image implementations. Then in Section 2-2, Non-negative Matrix Factorization (NMF) will be described in context of specular reflection removal.

## 2-1 Specular reflection removal methods

In this section relevant specular reflection removal methods from literature are described. The working principles behind the methods can differ strongly and it is evaluated how well they may perform on achromatic non-dielectric surfaces. First, in Section 2-1-1 single-image specular reflection removal methods and their working principles are investigated. Then, in Section 2-1-2 multi-image specular reflection removal methods are discussed.

### 2-1-1 Single-image specular reflection removal methods

Single image specular reflection removal methods generally aim to separate the specular component using colour or intensity information that is available from a single image. An advantage of single-image specular reflection removal methods is that they tend to require less complex image acquisition and have relatively fast implementations. In [3] single-image methods are classified as either color space analysis or neighbourhood analysis. Here the same classification is used with the added class of optimization based methods. Optimization based specular reflection removal methods have become more prevalent in recent literature.

In **color space analysis based specular reflection removal methods** the difference in color properties of the diffuse- and specular component are used to separate the two from

colored input images. In many methods the Dichromatic Reflection Model (DRM) is used to describe the RGB color of an arbitrary pixel,  $p$ :

$$\mathbf{i}_p = m_d \mathbf{i}_d + m_s \mathbf{i}_s. \quad (2-1)$$

In Equation (2-1),  $\mathbf{i}_p$ ,  $\mathbf{i}_d$  and  $\mathbf{i}_s$ , represent the colors of the pixel of the diffuse and specular component and they correspond to the relative spectral power distributions from Eq. (1-3). The weighting factors  $m_d$  and  $m_s$ , correspond to the respective diffuse and specular geometric scaling factors from Eq. (1-3). Clearly this equation cannot be easily solved, as the known term,  $\mathbf{i}_p$ , is a sum of the unknown diffuse and specular terms and the individual weighting factors and colors are both unknown as well. In [27] it was first proposed that pixels corresponding to an area on the surface with the same intrinsic diffuse color lie on the same plane in the RGB color space. This work was extended by Klinker et al. [16, 15, 17]. One of the main assumptions that is used is that pixels with the same pure diffuse color (with or without highlights) lie on a plane in the RGB color space spanned by the diffuse and specular color. This is illustrated in Figure 2-1. Moreover, it is assumed that the color of the specular reflected light is the same as the color of illumination. This implies the variable,  $\mathbf{i}_s$ , is known in Equation (2-1). Then, the diffuse color is estimated by fitting a color line to purely diffuse pixels that correspond to the same colored surface. After which the coefficients  $m_d$  and  $m_s$  can be computed using the position of the pixel in the plane spanned by  $\mathbf{i}_d$  and  $\mathbf{i}_s$ .

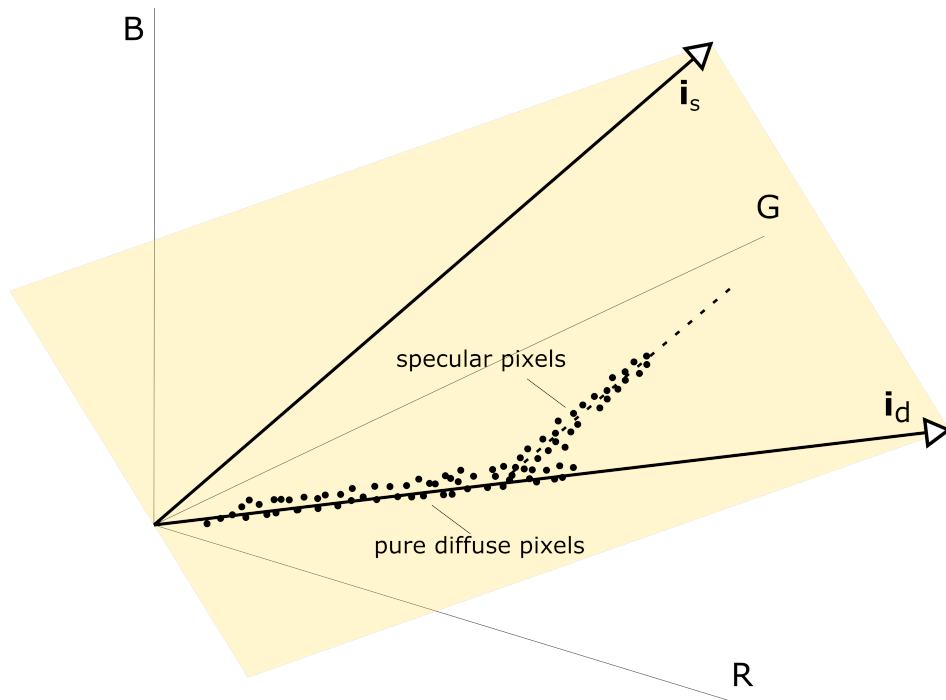


**Figure 2-1:** Pixel clustering in RGB color space of pixels from an image with a single diffuse color and a specular highlight. The pixels lie on the same plane spanned by the diffuse color direction,  $\mathbf{i}_d$ , and specular color direction,  $\mathbf{i}_s$ . (Figure after [15])

The color space analysis specular reflection removal methods have shown successful result for dielectric materials. However, they do suffer from a number of shortcomings and assumptions, that are more severe for non-dielectric materials. One problem is that for images with

saturated pixels the color estimation can fail, because some of the data is distorted. Also, the color space methods require some type of image segmentation into groups with the same diffuse color. Furthermore, the specular color is assumed exactly equal to the illumination color, which does not necessarily hold for non-dielectric materials at larger incident angles of illumination. The DRM is assumed, which is really only a valid model for non-dielectric materials at angles of incidence of illumination close to the surface normal. Additionally, color space analysis methods typically have trouble estimating the correct diffuse color when the diffuse color and specular color vectors are similar. Again this forms a problem for non-dielectric objects, because the often assumed white illumination color is close to the typically achromatic (grey) color of non-dielectric materials.

**Neighbourhood analysis based specular reflection removal methods** use local color- and/or intensity information to separate reflection components. Generally these methods have a simple and fast implementation. Moreover, it is often unnecessary to do any image segmentation for neighbourhood analysis type methods, because as opposed to color analysis based methods there is no assumption on the amount of diffuse colors present in the global image. Tan et al. [32, 31, 30] propose the *specular-to-diffuse mechanism*. This is based on the maximum of chromaticity and intensity values of diffuse and specular pixels. The main idea is that the maximum chromaticity of diffuse pixels will always be larger than that of specular points, under the assumption of white illumination. Furthermore it is shown that the specular points can be iteratively projected along a curve to its corresponding maximum diffuse chromaticity in order to eliminate specular reflection component. In general neighbourhood analysis specular reflection removal methods use local intensity differences and image specific thresholds for reflection component separation. This can result in better recovery of the surface texture. Again the DRM and white illumination is assumed, which makes neighbourhood analysis based methods less suitable for non-dielectric materials.

Recently, **optimization based specular reflection removal methods** have become more prevalent in literature. This type of method combines working principles from color space analysis and neighbourhood analysis type methods into one optimization framework. Typically, a model of the expected reflection is proposed and used to form an optimization problem, which is solved to identify and separate the diffuse and specular components of the model. Optimization based methods conclude to be applicable to a wider range of image scenes because of the global approach to the reflection separation problem. The global approach also implies there is automatic segmentation of the image into diffuse color groups. Akashi and Okatani [1] propose an optimization method for reflection separation using sparse NMF. The DRM is assumed and additionally it is assumed that there are only a finite amount,  $q$ , of diffuse colors present in the image. The results of [1] indicate that this optimization based approach can give satisfactory results for achromatic non-dielectric objects as well. The global approach ensures a more accurate estimation of the diffuse color, which makes this type of method more suitable for non-dielectric materials, because here typically the diffuse intensity is low compared to the specular intensity at the specular highlights. In Chapter 2 the method by [1] is described in more detail. In both [2] and [12] the Alternating Direction Method of Multipliers (ADMM) is used to solve a similar optimization problem. ADMM is particularly suitable for image manipulation problems since it can deal with large optimization problems in a robust manner and easily incorporate constraints within the optimization framework [6].

More recent optimization based specular reflection removal methods aim to improve separation performance further by incorporating more spatial priors into an optimization framework. For example, in both [20] and [10] the assumption that specular highlights are typically small in size and sparsely distributed in an image, is used as an additional constraint within an optimization framework. Similarly, in [13], improved results are obtained by using the additional prior information from a user that indicates which pixels contain specular reflections.

Single-image methods in general have shown to obtain excellent specular reflection removal results for dielectric materials. However, problems start to occur whenever a larger amount of different diffuse colors must be identified or when the specular highlights are no longer sparse. Different methods with additional global and local constraints have been proposed to solve this problem. Some are successful but typically the constraints imply that the method is only applicable to a small set of image scenes. Most single-image methods are based on the Dichromatic Reflection Model (DRM), which is only in limited cases applicable to non-dielectric materials. It has been found however, that some of the working principles of the single image specular reflection removal methods can still be effectively used for non-dielectric materials. This is constrained however to image scenes where the illumination is normal to the object surface. Especially optimization based specular removal methods have shown that they may be applied to non-dielectric materials as well, because of the global approach to the diffuse color estimation. Inherent to the problem, all single-image type methods are ill-posed. This may be solved using multiple image of the same scene, which will be investigated in the next section.

### 2-1-2 Multi-image specular reflection removal methods

Multi-image methods generally require a more complex imaging setup, but have more information available. This is advantageous because the separation of diffuse and specular reflection components from a single image is inherently an ill-posed problem. Most multi-image methods are based on the assumption that the diffuse component changes minimally with imaging geometry, while the specular component can completely disappear for different viewing or illumination angles.

Examples of multi-image specular reflection removal methods are [19] and [26]. Here multiple views of the same scene under the same illumination are used. A model is defined to explain the spectral difference (differences in color) between views. They show that the extra information available from the additional viewing angles can be used to separate specular reflection components. Moreover, it is shown that this method is less effective for non-dielectric surfaces, because the intensity of the diffuse reflection component is small and the specular highlights are often large in size. A simple multi-image method is proposed in [29]. Here feature correspondence between images of the same object are used to find the pixels corresponding to the same location on a object, after which the intensity is simply changed to the minimum value of corresponding pixels. The method described here all require enough images to ensure that from at least one viewing angle the image contains a purely diffuse pixel.

A different type of multi image specular reflection removal methods is based on the tendency

of the specular reflection components to be polarized. Recall that the polarization of reflected light is governed by two separate Fresnel ratio's for  $s$ - and  $p$ -polarized light. Assuming unpolarized incident light the specular reflected light can still be polarized dependent on the angle of incidence. Polarization based specular reflection removal methods like [36, 22, 21] all take multiple images of a scene through a polarization filter at different orientations. The intensity of pixels will change in between images if there is a (assumed polarized) specular reflection component. The diffuse reflection component is separated with help of the definition of an polarization ratio. Polarization based specular reflection removal methods are less effective for non-dielectric materials, because the polarization ratio is typically less distinctive compared to dielectric materials. This leads to incomplete separation of the specular reflection component.

In general multi-image specular reflection removal methods have shown to be able to identify the location of specular components much more accurately. Typically multi-image specular removal methods do not assume the Dichromatic Reflection Model (DRM). They can therefore be applied to images of non-dielectric materials without major false assumptions on the physics of light reflection. However, in multi-image methods the unrealistic assumption (especially for non-dielectric materials) is made that in one of the available images the intrinsic diffuse information is available undistorted by any specular component. In the limited case where a large number of images of an object from different viewpoints is available, polarization based specular reflection removal methods are very good at identifying and separating the specular reflection component from dielectric objects. Still the use of multiple images can be effective for the elimination of specular reflections from non-dielectric materials. Mainly because information from multiple images can be combined, to obtain more information on the diffuse reflection component, which is typically low in magnitude for non-dielectric materials.

## 2-2 Non-negative matrix factorization

In this section we first describe the model and optimization framework; Non-negative Matrix Factorization (NMF), in Section 2-2-1. In Section 2-2-2 we describe an optimization based method that successfully uses NMF for specular reflection removal.

### 2-2-1 Non-negative matrix factorization

In many data-analysis applications a better representation of the available data is desired. Non-negative Matrix Factorization (NMF) refers to such a representation of data but also to the problem of finding this representation [18, 14]. Consider a non-negative data matrix,  $M \in \mathbb{R}^{m \times n}$ . The goal is to find an approximate factorization of two non-negative factorization matrices, such that:

$$M \approx WH \tag{2-2}$$

In Eq. (2-2) the factorization matrices,  $W \in \mathbb{R}^{m \times p}$  and  $H \in \mathbb{R}^{p \times n}$ , are both non-negative and typically describe some characteristic property of the data. In [14] it is stated that the columns of  $W$  are basis vectors and can be thought of as 'building blocks' of the data and the coefficients in  $H$  describe how much each building block is present in parts of the data. Typically, NMF leads to a reduction of dimensionality and a more sparse representation of the data.

Generally, the problem of finding the factorization matrices is formulated as a minimization problem that minimizes the squared residual:

$$\min_{W, H \geq 0} \frac{1}{2} \|M - WH\|_2^2. \quad (2-3)$$

This is not a straightforward optimization problem since there are two unknowns. In fact this is an ill-posed bi-convex problem. A variety of methods have been proposed that solve the NMF optimization problem from Eq. (2-3). In [18] a relatively simple algorithm is proposed, where the factorization matrices,  $W$  and  $H$ , are alternately fixed such that two well-posed convex optimization sub-problems (in  $W$  and  $H$  alternately) remain. Those are then solved with relatively simple multiplicative update rules for  $W$  and  $H$ :

$$H^{k+1} = H^k \odot \frac{W^T M}{W^T W H} \quad (2-4)$$

$$W^{k+1} = W^k \odot \frac{M H^T}{W H H^T}. \quad (2-5)$$

In Eq. (2-4) and Eq. (2-5) the parameter,  $k$ , denotes the iteration and  $\odot$  describes the element-wise product. The non-negativity of both matrices is ensured by initializing them as such. The factorization matrices are iteratively updated until some convergence criteria is reached. It should be noted that there is ambiguity in the solution of Eq. (2-3), because scalings or permutations of solutions can approximate the same data matrix. However, this may be solved by adding additional constraints on the factorization matrices within the optimization problem. Because the factorization matrices represent characteristic properties of the data, the factorization may be improved further by smartly adding constraints to the optimization problem depending on the application. NMF is particularly suitable for image processing applications, since it give a more compact representation of the typically large data images, using color- and intensity factorization matrices. An example of NMF applied to specular reflection removal is given in the next section.

Often a regularization term is added to the NMF optimization problem. This ensures the noise present in the data image is partially ignored. Typically the 1-norm of one of the factorization matrices is added to the cost function, leading to the following optimization problem:

$$\min_{W, H \geq 0} \frac{1}{2} \|M - WH\|_2^2 + \rho \|H\|_1. \quad (2-6)$$

In Eq. (2-6)  $\rho$  is a regularization parameter, which has to be selected depending on the noise level in the data. This type of problem is referred to as sparse NMF.

### 2-2-2 Akashi and Okatani's specular reflection removal method

Akashi and Okatani [1] propose an optimization method for reflection separation using sparse Non-negative Matrix Factorization (NMF). The DRM is assumed and additionally it is assumed that there are only a finite amount,  $R$ , of diffuse colors present in the image. Each pixel can then be described as in Equation (2-7).

$$\mathbf{i}_p = \sum_{k=1}^R m_{d,k} \mathbf{i}_{d,k} + m_s \mathbf{i}_s \in \mathbb{R}^{+[3 \times 1]} \quad (2-7)$$

Again in Eq. (2-7),  $\mathbf{i}_p$ , represents the RGB pixel value and  $\mathbf{i}_d$  and  $\mathbf{i}_s$  are the diffuse- and specular normalized color vectors, respectively. It is additionally assumed that the specular color is known and white;  $\mathbf{i}_s = \frac{1}{\sqrt{3}}[1, 1, 1]^T$ . Eq. (2-7) is then written for all,  $N$ , total pixels in one equation as a non-negative matrix factorization.

$$M = WH \in \mathbb{R}^{+[3 \times N]} \quad (2-8)$$

In Eq. (2-8) the vectorized image,  $M \in \mathbb{R}^{3 \times N}$ , is written as the product of a matrix containing the colors present in a image and a coefficient matrix,  $W$  and  $H$ , respectively. They are defined below:

$$W = \begin{bmatrix} W_d & \mathbf{i}_s \end{bmatrix} \in \mathbb{R}^{+[3 \times (R+1)]},$$

$$H = \begin{bmatrix} H_d \\ H_s \end{bmatrix} = \begin{bmatrix} \mathbf{h}_{d,1} & \mathbf{h}_{d,2} & \dots & \mathbf{h}_{d,N} \\ m_{s,1} & m_{s,2} & \dots & m_{s,N} \end{bmatrix} \in \mathbb{R}^{+[(R+1) \times N]}.$$

Here,  $M$  is the vectorized image and  $W$  contains the illumination color and a finite number of unknown diffuse colors.  $H$ , is a matrix with unknown coefficients that represent how much their corresponding color is present for that pixel. Indeed Eq. (2-8) is an example of a NMF data representation. Following the DRM, in Eq. (2-7) it is assumed there can only be one non-zero diffuse coefficient for each pixel, which imposes a zero-norm constraint on the columns of  $H$ . This constraint is relaxed as a regularization term in the minimization function. Which gives the following optimization problem in [1]:

$$\min_{W_d, H \geq 0} \frac{1}{2} \|M - WH\|_2^2 + \rho \|H\|_1. \quad (2-9)$$

In Equation (2-9),  $\rho$  is a regularization parameter. It should be noted that the regularization term enforcing sparsity is exactly the same as the regularization term in Eq. (2-6), which ensures noise in the data is ignored. The regularization parameter in Eq. (2-9) should be selected dependent on both the noise level in the data and the desired degree of sparsity in the solution. Note that Equation (2-9) is an ill-posed bi-convex optimization problem. In [1] the problem is solved using alternating multiplicative update rules for  $W_d$  and  $H$ .

$$H^{k+1} = H^k \odot \frac{W^T M}{W^T W H + \rho} \quad (2-10)$$

$$W_d^{k+1} = W_d^k \odot \frac{V_l H^T + W_d \odot A W_d H H^T}{W_d H H^T + W_d \odot A V_l H^T} \quad (2-11)$$

Where in Eq. (2-11)  $V_l = M - \mathbf{i}_s H_s$ , which is added because only the diffuse basis vectors in  $W$  are updated. Moreover,  $\odot$ , indicates the entry-wise product and  $A$  is a  $3 \times 3$  matrix whose entries are all 1. In [8] the update rules are derived and the algorithm is shown to converge to a local minimum in finite iterations. Once the method has converged, a diffuse- and specular (vectorized) image can be reconstructed.

$$I_d = W_d H_d \quad (2-12)$$

$$I_s = \mathbf{i}_s H_s \quad (2-13)$$

Note that in the ideal case we have  $M = I_d + I_s$ , with the diffuse- and specular reflection component completely captured in the respective vectorized image.

In Figure 2-2 the results of the method from Akashi and Okatani [1] for both a dielectric and non-dielectric input image. All results were obtained using the MATLAB<sup>®</sup> implementation of the method provided by [25]. Note that for the dielectric object the specular highlights are correctly identified, and nearly completely eliminated from the diffuse image. The non-dielectric data-image contains more and brighter specular highlights. The specular highlights are only partially identified and the results are noisy. This is mainly caused by the fact that the diffuse signal is relatively weak compared to the specular component at the highlight. Moreover, the diffuse color of the non-dielectric object is closer to the assumed white specular color. However, the results for the non-dielectric object in Figure 2-2 do show that the method is able to accurately determine the diffuse color of the object and partially eliminate the specular reflection component.

### Dielectric object:



### Non-dielectric object:

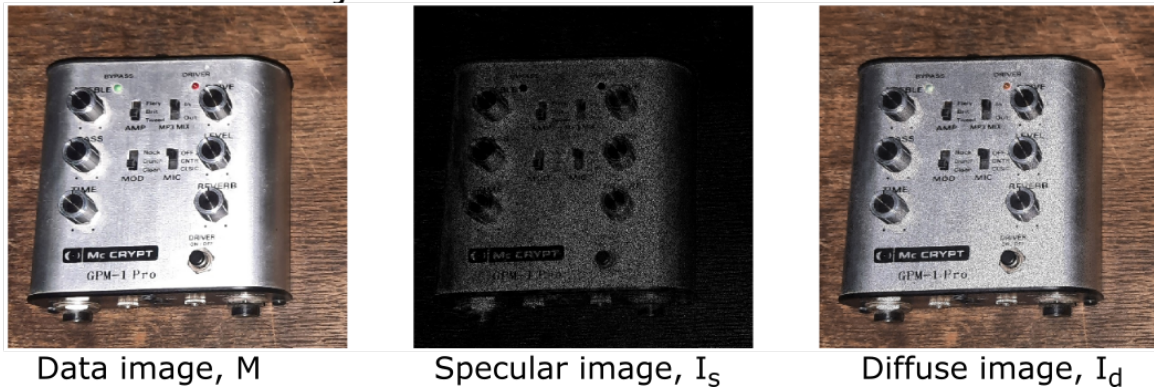


**Figure 2-2:** Results for the method in [1] for both a dielectric and non-dielectric object. The input image on the left is separated into a specular and diffuse image. Individual images are scaled for maximum contrast.

In this section NMF has been described to be a more sparse factorization of data using two characteristic factorization matrices. The factorization matrices are found by formulating an optimization problem, which also allows for easy incorporation of additional constraints on the factorization matrices. The results of the method in [1] show that NMF formulation is particularly useful within the context of specular reflection removal, because here we are interested in separating certain characteristic ‘building blocks’ of the data. Moreover, it shows that this approach to the specular reflection removal problem can even be applied to images of non-dielectric materials. NMF methods may be improved by adding additional constraints

representing prior knowledge on the factorization matrices to the optimization problem.

In this chapter it has been shown that there does not exist a specular reflection removal method with a simple imaging setup, that can successfully remove specular highlights from images of non-dielectric materials. Most single-image methods assume the Dichromatic Reflection Model (DRM), which is only a valid model for non-dielectric materials when the illumination direction is close to the surface normal. Additionally often white illumination and therefore a white specular color is assumed, which makes it harder to distinguish the typically achromatic color of non-dielectric materials. Multi-image method generally require a much more complex imaging setup, however they have shown adequate specular reflection removal even for non-dielectric materials. The main advantage is that multi-image methods provide more information on the diffuse signal, which is relatively low in magnitude for non-dielectric materials. In the next chapter a new model and specular reflection removal methods is described, which aims to avoid the shortcomings of existing methods.



# Multi-image optimization based specular reflection removal for non-dielectric objects

In this chapter a new specular reflection removal method and the main contribution of this thesis is described. A multi-image optimization based specular reflection removal method is proposed specifically designed to work for the removal of specular highlights from non-dielectric materials. First in Section 3-1 the surface reflection model used within the method is described, together with the physical assumptions that are made. Then in Section 3-2 the description of the proposed specular reflection removal method is given.

### 3-1 Surface reflection model

This section gives a detailed description of the surface reflection model used within the method. This model is an extension of the model proposed by [1] from Eq. (2-7). It aims to deal with two problems with specular reflection that were identified in the previous chapters. Firstly, the model does not require white illumination/ specular color, which makes the typically achromatic non-dielectric colors easier to distinguish. Moreover, the model is formulated in such a way that it can be extended for multiple input images, which allows for more available information on the diffuse- and specular image.

Again the Dichromatic Reflection Model (DRM) is assumed, which indicates that the surface reflection consists of a diffuse- and specular reflection component. And the diffuse color therefore originates from the initially transmitted incident light, after which it is re-emitted with a different spectrum, because the absorption within the material is wavelength dependent. Similar to other specular reflection methods the specular reflection color is assumed known and equal to the illumination color. However, in this case we do not assume the illumination

is white, which allows for a different formulation of the pixel values. The following model for the pixel values is proposed:

$$\mathbf{i}_p = \sum_{k=1}^R m_{d,k} \mathbf{i}_{d,k} \odot \mathbf{i}_s + m_s \mathbf{i}_s \in \mathbb{R}^{+[3 \times 1]}. \quad (3-1)$$

Note that Eq. (3-1) is similar to the description used by [1] in Eq. (2-7), however now the diffuse component has the color of the true normalized diffuse color vector,  $\mathbf{i}_d$ , projected onto the known normalized specular color vector,  $\mathbf{i}_s$ . This is denoted by the element-wise product,  $\mathbf{i}_{d,k} \odot \mathbf{i}_s$ . Again we assume that there are,  $R$ , diffuse colors present in the image and we can write Eq. (3-1) simultaneously for all,  $N$ , pixels of the vectorized image,  $M \in \mathbb{R}^{3 \times N}$ :

$$M = \mathbf{i}_s \odot WH = \mathbf{i}_s \odot \begin{bmatrix} 1 \\ 1 \\ 1 \end{bmatrix} H_s + \mathbf{i}_s \odot W_d H_d \in \mathbb{R}^{[3 \times N]}. \quad (3-2)$$

The factorization matrices now then defined with:

$$W = \begin{bmatrix} \mathbf{1} & W_d \end{bmatrix} = \begin{bmatrix} \mathbf{1} & \mathbf{i}_{d,1} & \dots & \mathbf{i}_{d,R} \end{bmatrix} \in \mathbb{R}^{[3 \times (1+R)]},$$

$$H = \begin{bmatrix} H_s \\ H_d \end{bmatrix} \in \mathbb{R}^{[(1+R) \times N]}.$$

Note that in Eq. (3-2) the only unknowns are  $H$  and  $W_d$ .

Another important proposition to improve the specular reflection removal performance is to use multiple input images. A number of assumptions are made on the different sub-images used as inputs. Firstly, the same scene is captured under the same illumination direction and with the same illumination intensity for all sub-images. This, together with the assumption that the specular reflection is equal for all wavelengths, ensures that within the sub-images the specular highlights have the same intensity profile. Or equivalently,  $H_s$  is the same for all sub-images. Furthermore, because the illumination intensity in between sub-images is the same and because the diffuse color is an intrinsic property of the object, we can assume the diffuse factorization,  $W_d H_d$ , is the same for all sub-images. Also note that it is assumed that the scene for each sub-image is of a single illumination color. For images captured under these conditions, we can rewrite the model for an arbitrary sub-image with subscript  $i$ :

$$M_i = \mathbf{i}_{s,i} \odot WH = \mathbf{i}_{s,i} \odot \begin{bmatrix} 1 \\ 1 \\ 1 \end{bmatrix} H_s + \mathbf{i}_{s,i} \odot W_d H_d \in \mathbb{R}^{+[3 \times N]}. \quad (3-3)$$

In Eq. (3-3) the same non-negative matrix factorization,  $WH$ , is projected with an elementwise product with  $\mathbf{i}_{s,i}$ , to the corresponding  $i$ 'th sub-image. Note that this model implies that each sub-image only contains partial information on the diffuse image,  $I_d = W_d H_d$ , and the specular

intensity profile,  $\begin{bmatrix} 1 \\ 1 \\ 1 \end{bmatrix} H_s$ .

## 3-2 Multi-image optimization based specular reflection removal for non-dielectric objects

This section describes a new multi-image sparse non-negative matrix factorization specular reflection removal method for non-dielectric objects, based on the model in Eq. (3-3) from Section 3-1. The problem of specular reflection removal is posed as an optimization problem and solved by alternately solving two sub-optimization problems.

Suppose we have  $q$  input images, the goal is to find a factorization that minimized the residual error with the data for all sub-images, while also ensuring that the factorization can be split into specular- and diffuse reflection components. The following optimization problem is proposed:

$$\min_{W_d, H \geq 0} J_1 = \sum_{i=1}^q \|M_i - \mathbf{i}_{s,i} \odot (\mathbf{1}H_s + W_d H_d)\|_2^2 + \rho \|H\|_1 \quad (3-4)$$

In Eq. (3-4) we essentially try to simultaneously minimize the  $q$  different data-residuals of the sub-images with the color projected non-negative matrix factorization. As in [1] we again add a regularization term on the coefficient matrix  $H$ , which functions as regularization of possible noise in the data but also ensures sparsity of the solution. Eq. (3-4) again forms an ill-posed bi-convex optimization problem, which can be solved using iterative alternating sub-optimization problems. In this method we define the following iterative steps, with  $k$  denoting the current iteration:

$$H^{k+1} = \min_{H \geq 0} \left( \sum_{i=1}^q \|M_i - \mathbf{i}_{s,i} \odot (\mathbf{1}H_s + W_d^k H_d)\|_2^2 + \rho \|H\|_1 \right), \quad (3-5a)$$

$$W_d^{k+1} = \min_{W_d \geq 0} \left( \sum_{i=1}^q \|M_i - \mathbf{i}_{s,i} \odot (\mathbf{1}H_s^{k+1} + W_d H_d^{k+1})\|_2^2 + \rho \|H^{k+1}\|_1 \right), \quad (3-5b)$$

$$W_d^{k+1}(:, j) \leftarrow \frac{W_d^{k+1}(:, j)}{\|W_d^{k+1}(:, j)\|_2} \quad \text{for } j = 1, \dots, R. \quad (3-5c)$$

The sub-optimization problems in Eq. (3-5a) and Eq. (3-5b) are both constrained quadratic optimization problems, which can be efficiently solved. Note that the update for the coefficient matrix,  $H$ , is separable in its columns, which implies the intensity coefficients are estimated pixel-wise. The iterative update for the diffuse color matrix in Eq. (3-5b) is separable in its rows (i.e. color channels). In Eq. (3-5c) the columns of  $W_d$  are normalized after each update for the factorization matrices. This step is added to eliminate the ambiguity in the scale of the solution. In [8] it was shown that this normalization step does not affect the solution.

Note that similar to the implementation in [1], the regularization parameter,  $\rho$ , serves a double purpose. It serves as regularization of possible noise in the data but also ensures sparsity of the diffuse color selection by putting extra weight on the columns of  $H$ . However, really the sparsity regularization term should only be put on the columns of the diffuse coefficient matrix  $H_d$ . Therefore, it is proposed to separate the regularization on the diffuse and specular coefficients. We obtain the following optimization problem:

$$\min_{W_d, H \geq 0} J_2 = \sum_{i=1}^q \|M_i - \mathbf{i}_{s,i} \odot (\mathbf{1}H_s + W_d H_d)\|_2^2 + \rho_s \|H_s\|_1 + \rho_d \|H_d\|_1 \quad (3-6)$$

In Eq. (3-6) the specular- and diffuse regularization parameters,  $\rho_s$  and  $\rho_d$  respectively, can now be individually determined. The following iterations are used to solve the problem:

$$H^{k+1} = \min_{H \geq 0} \left( \sum_{i=1}^q \left\| M_i - \mathbf{i}_{s,i} \odot (\mathbf{1}H_s + W_d^k H_d) \right\|_2^2 + \rho_s \|H_s\|_1 + \rho_d \|H_d\|_1 \right), \quad (3-7a)$$

$$W_d^{k+1} = \min_{W_d \geq 0} \left( \sum_{i=1}^q \left\| M_i - \mathbf{i}_{s,i} \odot (\mathbf{1}H_s^{k+1} + W_d H_d^{k+1}) \right\|_2^2 \right), \quad (3-7b)$$

$$W_d^{k+1}(:, j) \leftarrow \frac{W_d^{k+1}(:, j)}{\|W_d^{k+1}(:, j)\|_2} \quad \text{for } j = 1, \dots, R. \quad (3-7c)$$

Note, that now in Eq. (3-7b) the regularization terms are omitted because they do not affect the solution.

To initialize the implementation all known variables are loaded. All data matrices  $M_i$  and the normalized specular color vectors,  $i_{s,i}$ , are assumed known. The factorization matrices are initialized randomly. The coefficient matrix,  $H$ , is initialized with uniformly distributed random numbers over the range [0,255] for 8-bit input images. The values of the entries of the diffuse color matrix,  $W_d$ , are initialized with random positive values, after which the columns are normalized. Then the iterations in Eq. (3-7) are executed until some convergence criteria is reached. The iterations will be stopped when the relative change in the cost function value is smaller than a convergence threshold,  $\epsilon$ , or if the iteration count reaches a predefined maximum.

In this method a number of parameters must be selected. Firstly, the amount of input images to be used should be selected. It is expected that using more input images will result in better results, because it provides more information on the reflection components. However, this does require a more work in acquiring the data and the implementation is more computationally intensive. Note that the increase in computational time is marginal, because the amount of optimization variables in Eq. (3-6) is independent on the amount of input images. Moreover, the number of diffuse color vectors,  $R$ , should be determined beforehand. Typically, this can be set by the user, by estimating the amount of diffuse color present in the imaged scene. In [1] it was shown that there is no significant difference in results for a range of,  $R$ . Still this parameter should be determined according to the diffuse colors present in the imaged scene. We have two regularization parameters that should be selected. Both  $\rho_s$  and  $\rho_d$  should be selected according to the noise present in the image, but they also account for the sparsity of the specular- and diffuse component, respectively. This is not a straightforward selection, because it is strongly dependent on the magnitude of noise-, specular- and diffuse signals in the imaged scene.

In this chapter a new specular reflection removal methods is proposed. The proposed reflection model can be used to model multiple input images as a projection of the specular and intrinsic diffuse reflection components onto the specific illumination colors. The unknown variables are estimated by posing the model as a sparse Non-negative Matrix Factorization (NMF) problem. The resulting ill-posed bi-convex optimization problem is solved using alternating regularized quadratic sub-optimization problems. The method is designed in such a way that

it can also be used for the specular reflection removal from non-dielectric materials. Similar working principles as in the color-space and optimization based method discussed in Section 2-1 are used, however now they are extended to allow for more distinct available information, through multiple input images and colored illumination. The next chapter will discuss the experiment and results used for the evaluation of the proposed method.



# Results and discussion

In this chapter we will evaluate the multi-image optimization based specular reflection removal method for non-dielectric materials proposed in Chapter 3. First in Section 4-1 the different experiments that are used will be described, together with the method of evaluation. Then in Section 4-2 the experiment results and interpretation of results is given. General observations on the results are given in Section 4-3.

### 4-1 Experiment description

In this section the experiments performed in order to evaluate the proposed method are described. The method is tested on captured images of non-dielectric materials in a lab environment and on a synthetic data set. First in section Section 4-1-1 the type of data and image scene is described together with the manner of acquiring the data. In Section 4-1-2 the way of evaluating the results is described.

#### 4-1-1 Data acquisition

Following the description of the reflection model and specular reflection removal method in Chapter 3, we have a number of constraints on the data. A suitable set of input images must display exactly the same scene. The illumination colors have to be known and the illumination intensity should be equal for all images. There should be one unique illumination color per sub-image. Additionally, the data should contain minimal saturated pixels, because otherwise the reflection model fails. Because we focus on non-dielectric materials and assume the Dichromatic Reflection Model (DRM), it is especially important that both the illumination direction and the observer direction are close to the surface normal. Such image sets are not readily available online. Therefore, an experimental setup has been used to obtain a number of image sets for actual objects. Also, a synthetic data set is created, such that we have an image set that is completely conform the proposed reflection model.

The real data sets are obtained in a lab environment, that can be completely obfuscated. For the colored illumination, a THORLABS<sup>®</sup> LIU365A LED array light source is used together with a set of dichroic color filters. A 12-bit camera, *UI-3060CP-C-HQ Rev.2*, and short focus lens, *IDS-10M11-C1616*, from IDS-Imaging<sup>®</sup> are used. The images are captured using the *uEye Cockpit*<sup>®</sup> software. A number of different non-dielectric materials are used as sample. When capturing the data it is made sure that all camera parameters in between images are the same, and saturation is avoided. In Figure 4-1 an indicative picture of the setup is given.

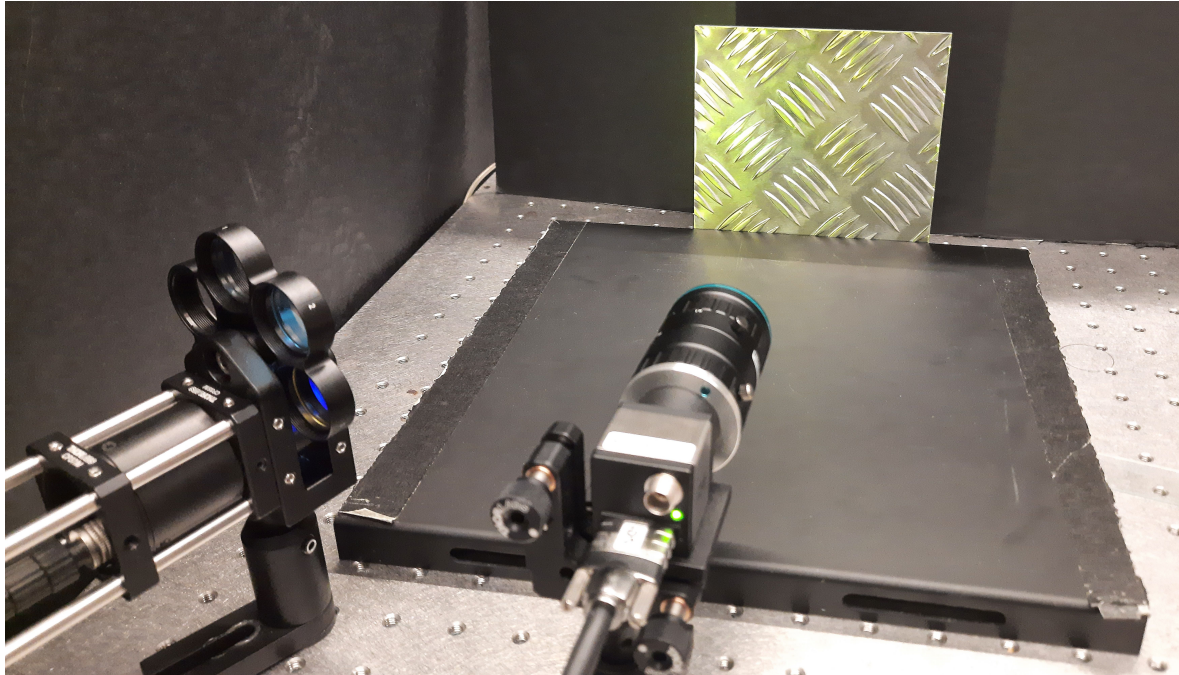


**Figure 4-1:** Overview of the experimental setup for acquiring data images of non-dielectric objects. A non-dielectric sample is illuminated by a (color-filtered) LED-array illumination. The images are captured by a scientific camera positioned in the direction of the sample surface normal. Note that for acquisition of the actual data sets the room illumination is switched off and the camera/illumination source positions are different.

Recall that within the implementation it is assumed that the specular color vectors are known and have the same color as the illumination color. We therefore must identify the specular colors corresponding to our setup. The white LED-array has a certain illumination spectrum, which combined with the transmission spectrum of the color filters define the illumination spectrum. In order to obtain a set of known illumination colors in RGB-space, the illumination source can be directly image by the camera. Then we can compute the average RGB values, to obtain the illumination color in RGB-space. Note that the different illumination spectra do not necessarily have the same intensity. Therefore, the average intensity is also registered and used to scale the input sub-images in pre-processing, such that they all have the same illumination intensity. In Figure 4-2 the resulting images of the illumination source, together with their average normalized RGB-color vector and relative average intensity are shown.

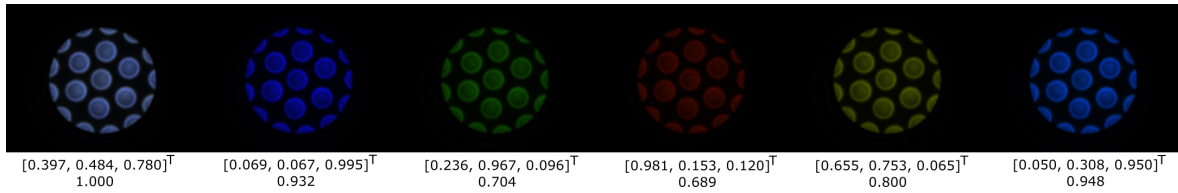


**Figure 4-2:** Set of images of the color-filtered LED-array illumination source used within the experiment. The corresponding normalized average RGB-color and relative average intensity with respect to the white illumination source are shown. These colors are used within the implementation as the known normalized specular color vectors.

It is difficult to obtain the ground truth of the diffuse reflection component for the image set of actual non-dielectric objects. Therefore, it is proposed to use a synthetic data set for which the ground truth is known. Moreover, we can create the synthetic data set in such a way that it is completely conform the model from Section 3-1.

A synthetic circular object with three regions of different diffuse colors is generated. It is assumed the synthetic illumination generates a circular patch of uniform intensity overlapping the three diffuse color regions. In Figure 4-3 the image and composition of the generated data set is given. The diffuse intensity is set much weaker relative to the specular intensity, since this is typical for non-dielectric materials. Additionally, a small noise signal is added to the data to mimic the acquisition of data within an actual imaging setup. The relative intensities of the specular- diffuse- and noise signal are set to 0.8, 0.2 and 0.01, respectively. For easier comparison, the specular colors are picked from the illumination colors which were identified in Figure 4-2.

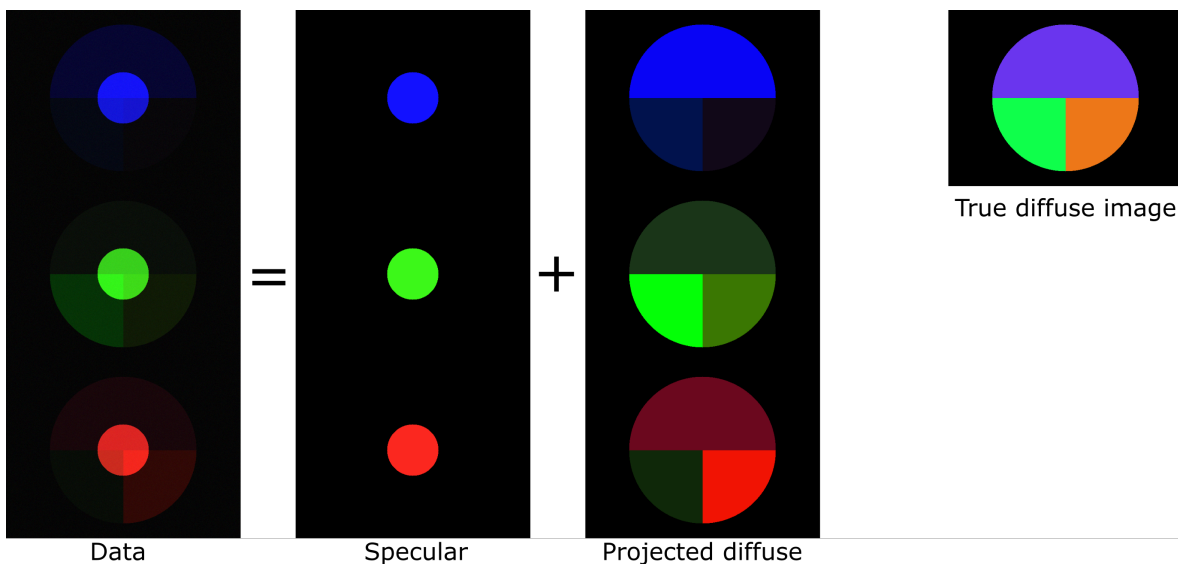


**Figure 4-3:** Overview of the generated synthetic data set. The true diffuse image (top-right) is assumed to be uniformly illuminated with different illumination colors equal to the specular colors, which gives the projected diffuse images. The projected diffuse images summed with the specular images gives the data images, which can be used as input within the implementation. Note that the intensity of individual images is scaled for maximum contrast.

### 4-1-2 Evaluation method

It is important to show the effectiveness of the proposed method in removing the specular reflection component and recovering the intrinsic diffuse image. A problem is that we do not have a good way of acquiring the ground truth for the diffuse image, approximated in the implementation by  $I_d = W_d H_d$ . If the ground truth diffuse image is not available we can still do an informative evaluation with visual comparison. The localization of specular highlights can be evaluated in this way. And using visual inspection together with the numerical results for the specular- and diffuse coefficients in  $H_s$  and  $H_d$ , it should also be clear if the algorithm succeeds in eliminating the specular reflection component at least partially. We can also use a multi-image method similar to [26], where a specular-free image is obtained by taking a lot of images from different orientations with a fixed illumination direction. However, the diffuse intensity profile will not match the data for the specular reflection method, but assuming we have a sample consisting of one diffuse color, we can use the average color of the reconstructed image for validation of the diffuse color estimation by our implementation.

We should also test the sparsity of the columns of the diffuse coefficient matrix,  $H_d$ , because the DRM is assumed, which implies for each column of  $H_d$  there is only one non-zero entry. To test this we use the average sparsity metric defined in Eq. (4-1) based on the sparseness measure from [14]. Recall that  $H_d \in \mathbb{R}^{R \times N}$ , where  $R$  is the amount of diffuse color vectors and  $N$  the amount of pixels per sub-image. The  $i$ 'th column of  $H_d$  is denoted by  $\mathbf{h}_{d,i}$ . The metric ranges from 0, to perfect sparsity at a value of 1.

$$\text{sparseness}(H_d) = \frac{1}{N} \sum_{i=1}^N \frac{\sqrt{R} - (\sum \mathbf{h}_{d,i}) / \|\mathbf{h}_{d,i}\|_2}{\sqrt{R} - 1} \quad (4-1)$$

For the synthetic data-set the ground-truth is available, and we can use quantitative performance metrics. A commonly used measure in image reconstruction evaluation is the Mean Squared Error (MSE). Additionally in [35] the Structural Similarity Index (SSIM) is proposed, which provides an indication of the performance of the structural recovery of the reference image. This measure ranges from 0 to 1 at perfect recovery of the reference image. In Section 4-2-1 the Mean Squared Error (MSE) and Structural Similarity Index (SSIM) will be used to compare the recovered diffuse image to the ground truth.

## 4-2 Experimental results

In this section a number of experiments are performed in order to evaluate the optimization based multi-image specular reflection removal method for non-dielectric materials, proposed in Chapter 3. First in Section 4-2-1 the method is tested on a synthetic data set, where the performance of the method is evaluated using quantitative measures and visual comparison. Moreover, the sensitivity to parameters in the implementations is investigated. In Section 4-2-2 the method is tested on the captured data sets of non-dielectric samples. It should be noted that for all experiments we set a fixed convergence threshold,  $\epsilon = \exp(-15)$  and for experiments with the same data set the factorization matrices  $W_d$  and  $H$ , are initialized with the same random matrices.

### 4-2-1 Results for synthetic data sets

First the proposed method is tested on the synthetic data set from Figure 4-3. This implies we have three input images, with three known illumination colors. The true diffuse image consists of a circular patch with three different diffuse color regions. We set  $R = 3$ , and the specular- and diffuse regularization terms are set to the best empirically found values;  $\lambda_s = 1$  and  $\lambda_d = 3$ , respectively. The known specular colors are set to the same colors as in the lab experiment as identified in Figure 4-2. The results are given in Figure 4-4 and Figure 4-5. The resulting images can visually be compared with the images from Figure 4-3.

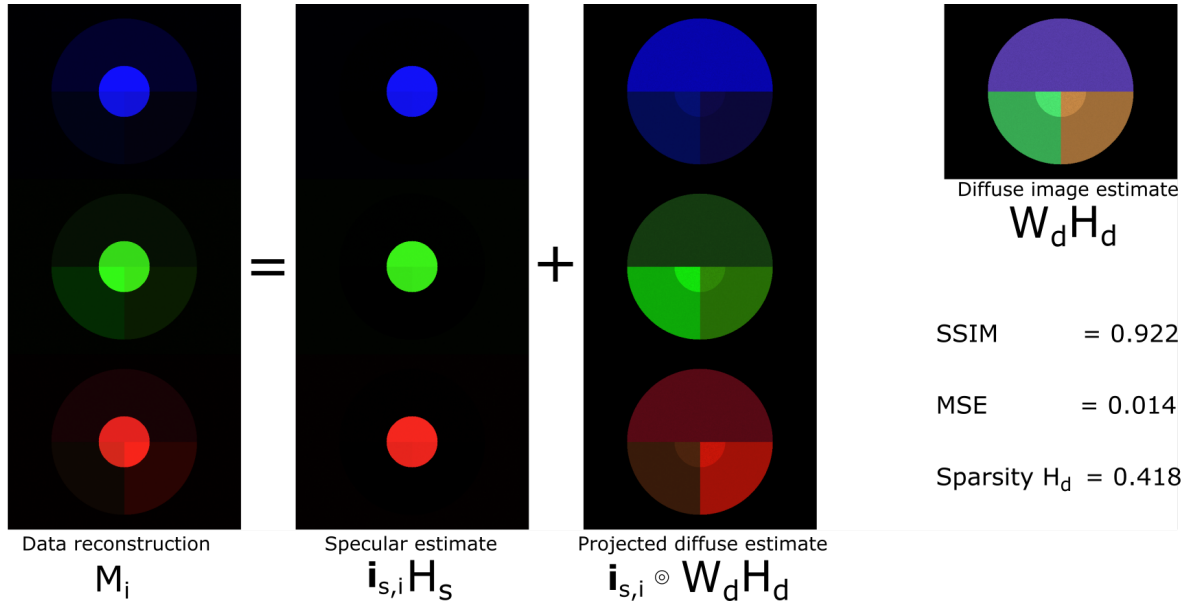


**Figure 4-4:** Results for synthetic data set as input, with three input images and  $R = 3$ ,  $\rho_s = 1$  and  $\rho_d = 3$ . The intensity of individual images is scaled for contrast.

From the results it immediately becomes apparent that the proposed method succeeds in separating the specular- and diffuse reflection component. Looking closer at the diffuse image estimate in Figure 4-4, we do observe some intensity differences at the location of the specular highlight, and the results are noisy. The small MSE value and SSIM index show that the diffuse image is a close representation of the ground truth. Note that the specular- and diffuse regularization parameters,  $\rho_s$  and  $\rho_d$ , are unequal. Both parameters are to be selected dependent on the noise in the image versus the amount and intensity of the specular- or diffuse reflection component in the image, respectively. Additionally, a larger diffuse regularization parameter is preferred because this ensures the column sparsity of  $H_d$ . However, if the ratio between the two regularization parameters is too large, the algorithm will end up trying to explain the data as solely specular or solely diffuse, and no reflection component separation is obtained. The individual normalized diffuse color vectors are not an accurate estimation of the actual diffuse colors. We have:

$$W_d = \begin{bmatrix} 0.435 & 0.791 & 0.284 \\ 0.302 & 0.544 & 0.862 \\ 0.848 & 0.279 & 0.419 \end{bmatrix}, \quad \text{TRUE } W_d = \begin{bmatrix} 0.398 & 0.891 & 0.056 \\ 0.199 & 0.445 & 0.958 \\ 0.896 & 0.089 & 0.281 \end{bmatrix}.$$

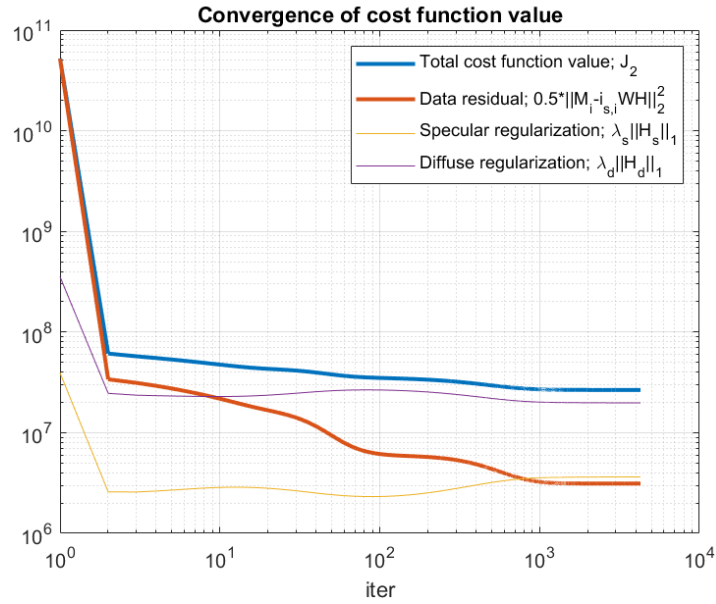


**Figure 4-5:** Double logarithmic convergence results for the synthetic data set with 3 input images. The total cost function value  $J_2$  from Eq. (3-6) shows a decreasing behaviour and the convergence criteria is reached after 4280 iterations in 1561 seconds.

This is mostly due to the fact that the average column sparsity of  $H_d$  is very low (0.418). The convergence plot in Figure 4-5 shows a gradual decline of the cost function value and residual of the data with the reconstructed factorization. The sum of the regularization term stays approximately equal during the optimization. This particular simulation converged in 4280 iterations after 1561 seconds. The simulation time is strongly dependent on the random initialization of the factorization matrices.

We can test the added value of using more input images by using a ground truth data set with additional input sub-images with different illumination colors. We now use the same synthetic data set as before, with two added sub-image with different illumination colors.

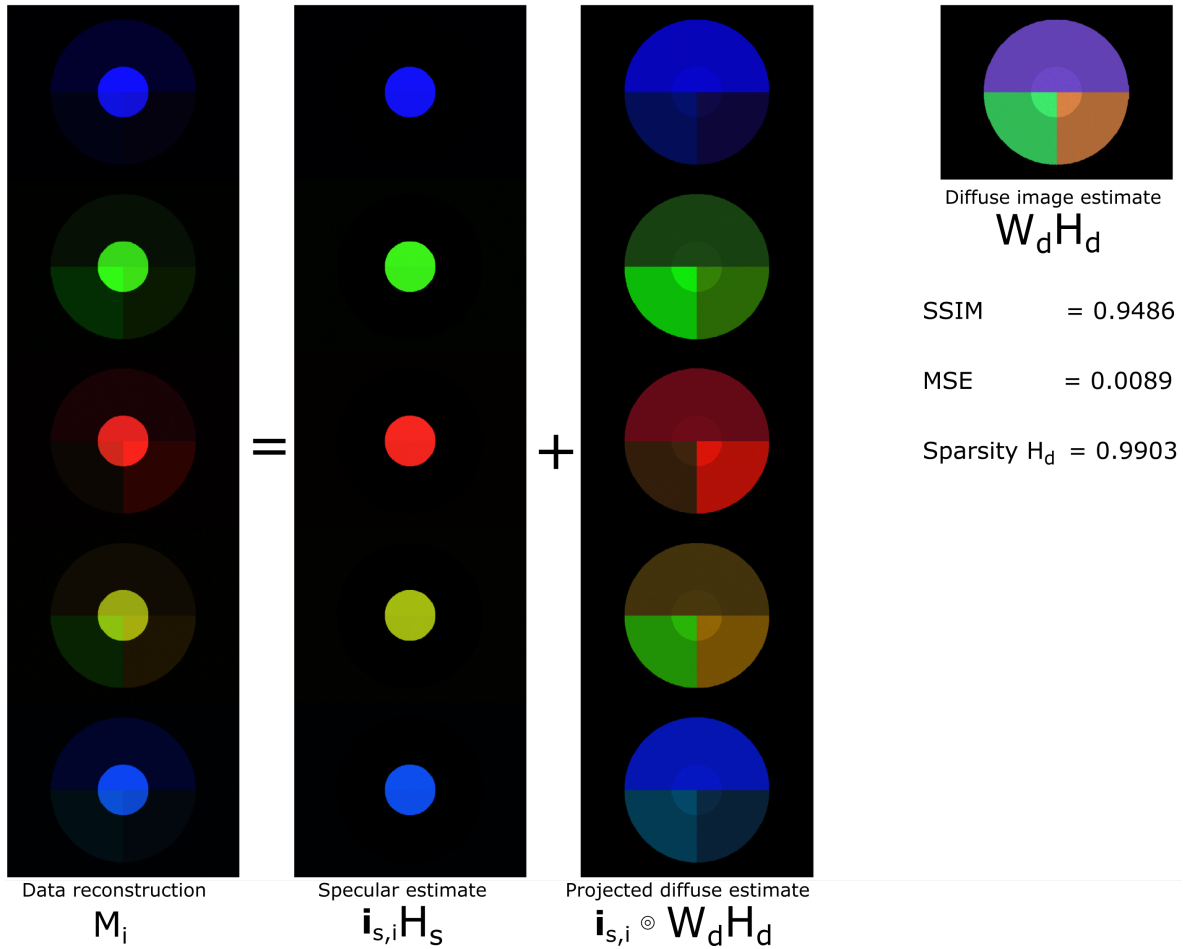


**Figure 4-6:** Results for synthetic data set as input, with five input images and  $R = 3$ ,  $\rho_s = 1$  and  $\rho_d = 3$ . The intensity of individual images is scaled for contrast.

The results in Figure 4-6 show only a slight improvement in reconstruction of the diffuse image. The SSIM index is somewhat higher and MSE now equals 0.009. We observe that adding more input images does not improve the results significantly, if the set of illumination colors already illuminate all color channels. The algorithm converged in 2687 iterations after 1860 seconds. This indicates that the simulation time does not increase significantly when using more input images. This is due to the fact that the amount of optimization variables is independent of the number of input images.

In Section 3-2 it was mentioned that the specular- and diffuse regularization parameters,  $\rho_s$  and  $\rho_d$ , should be carefully selected according to a number of properties of the data. To test the sensitivity of the method to these two parameters, we run the same experiment as in Figure 4-4 for several combinations of values for the two regularization parameters. The resulting recovered diffuse image, together with performance metrics is shown in Figure 4-7.

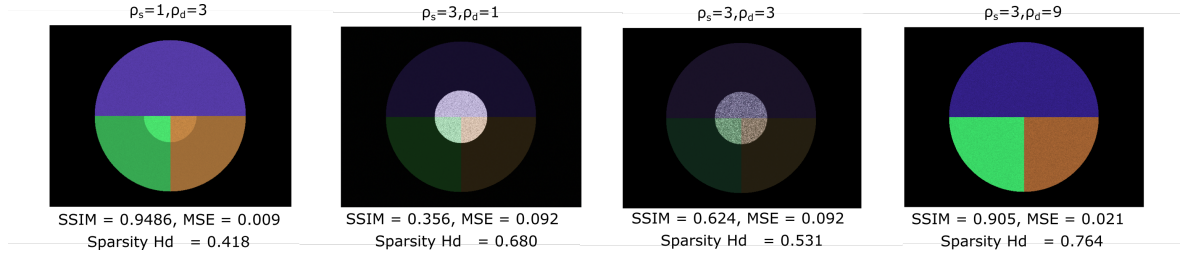


**Figure 4-7:** Recovered diffuse image ( $W_d H_d$ ) for different combinations of the specular- and diffuse regularization parameters,  $(\rho_s, \rho_d)$ . Additionally, the Structural Similarity Index (SSIM), the Mean Squared Error (MSE) and average column sparsity of  $H_d$  are given.

From Figure 4-7 we observe that the recovered diffuse image is sensitive to the regularization parameters. The magnitude of the regularization parameters both should match the noise present in the image. For this data set we know the mean of the noise signal is equal to 2.55, and therefore values for the regularization parameter in this order of magnitude are suitable. However, a distinction between specular- and diffuse regularization was implemented. This implies the ratio of the specular- and diffuse regularization parameter values should represent the ratio or sparsity of specular and diffuse reflection component present in the data. From the results in Figure 4-7, we observe that the ratio,  $\rho_s/\rho_d \approx 1/3$ , is suitable. Namely, for  $(\rho_s = 3, \rho_d = 1)$  and  $(\rho_s = 3, \rho_d = 3)$  the algorithm prefers the diffuse reflection components and falsely explains some of the specular reflection component to be diffuse. Visually, the parameter set  $(\rho_s = 3, \rho_d = 9)$  seems to give a better result, because the artefact in the location of the specular highlight has disappeared. However, the result is noisy and the diffuse color estimation is less accurate, which is indicated by the deteriorated values for the MSE and SSIM. By increasing the diffuse regularization parameter to  $\rho_d = 9$ , we indeed can confirm the ideal model is followed more accurately. Now the average column sparsity of  $H_d$  equals 0.764.

Another test, where only one synthetic input image with blue illumination is used, failed to give a good reconstruction of the diffuse image. Mainly, because there was effectively only information available on the blue color channel. It is thus important to select illumination colors that together cover all color channels and of which at least one is dissimilar from the diffuse colors.

#### 4-2-2 Results for non-dielectric data sets

In this section the proposed method from Chapter 3 is tested on non-dielectric data sets. The data images are acquired in a lab environment as described in Section 4-1-1.

Figure 4-8 shows the first data set with images of an **aluminum plate with profile**, used to test the method. The images are very dark, this is because the relative intensity of the specular highlights are much larger compared to the mean diffuse signal in the image. For clarity all results will be shown with gamma correction,  $\gamma = 2$ , and the intensity is scaled for maximum contrast.

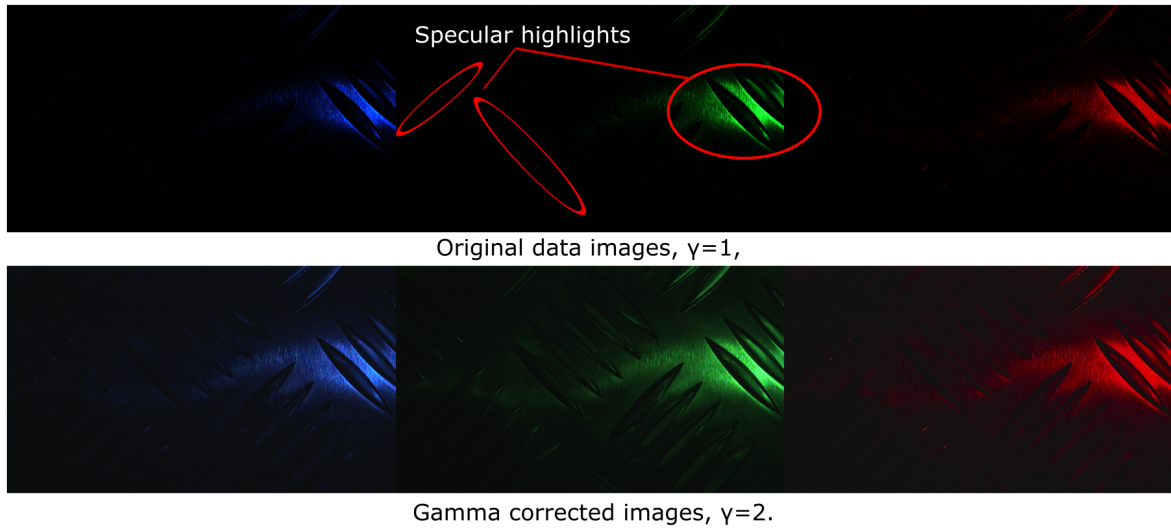


**Figure 4-8:** Acquired data images of a non-dielectric aluminum plate with profile. Both the original images and gamma corrected ( $\gamma = 2$ ) data is shown. Multiple specular highlights appear on the edges of the profile and one larger specular highlight is present on the main surface. The location of specular highlights are indicated in the green sub-image. The images are scaled for maximum contrast.

For the simulation we first fix the parameters of the method. Again we set the convergence threshold to  $\epsilon = \exp(-15)$ . The data images are of a single object with a single color so we let  $R = 1$ . The regularization parameters are empirically set to the following values:  $\rho_s = 2$  and  $\rho_d = 1$ . The results are given in Figure 4-9 and Figure 4-10.

The first thing we can observe from Figure 4-9 is that the algorithm is able to accurately reconstruct the data input images, by comparing it with the gamma corrected images in Figure 4-8. In the specular image estimate, we observe that the algorithm has identified the large specular highlight on the main plate surface, and also the smaller highlights on the profile edges are identified. Looking at the projected diffuse image estimate in Figure 4-9, we observe that a significant portion of the specular reflection components have been eliminated. An exact quantification of this cannot be given, because there is no ground truth data available on the individual reflection components. In the brightest part of the larger specular highlight, the diffuse image estimate shows zero intensity pixel value and thus fails to give a correct reconstruction. This is caused by the fact that here the data images have saturated pixel values, and thus the reflection model and optimization algorithm fails. An indication of the accuracy of the diffuse color estimation can be given by determining the diffuse color in an alternate manner with a multi-image method as described in Section 4-1-2. We find:  $\text{TRUE } W_d = [0.429, 0.523, 0.736]^T$ , which is close to the estimated diffuse color,  $W_d = [0.522, 0.464, 0.716]^T$ .

The convergence results are shown in Figure 4-10, they indicate a faster convergence compared to the synthetic data set, caused by the fact that we now only have one unknown diffuse color,  $R = 1$ . But again the convergence speed strongly depends on the random initialization of the matrix factorization.

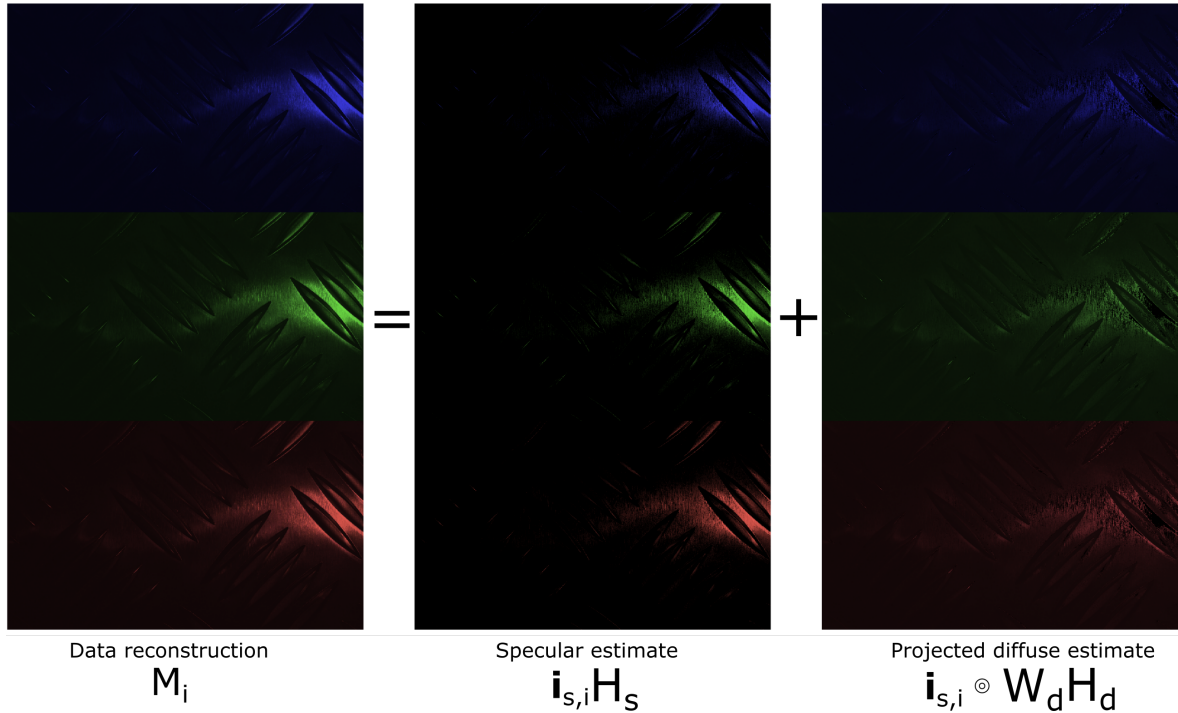


**Figure 4-9:** Results for input data images of a non-dielectric aluminum profile plate, with parameters set to  $R = 1$ ,  $\rho_s = 2$  and  $\rho_d = 1$ . The data is reconstructed through the summation of a specular image and projected diffuse image estimate. The specular estimate image indicates a correct localization of the specular highlights in the data.

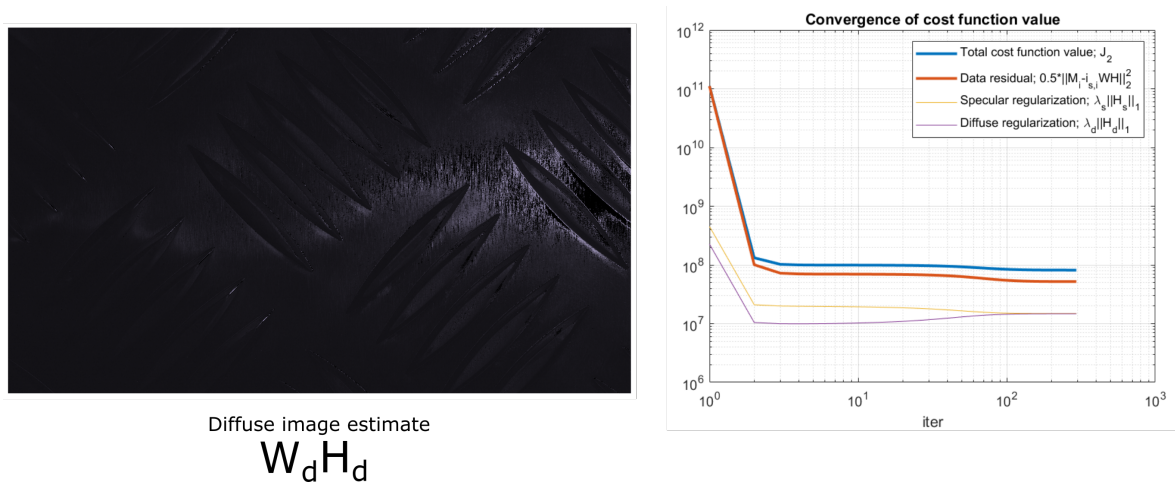


**Figure 4-10:** Left: Reconstructed diffuse image ( $W_d H_d$ ) of the non-dielectric aluminum profile, corresponding to the results in Figure 4-9. The image is gamma corrected ( $\gamma = 2$ ) and scaled for maximum contrast. Right: Double logarithmic convergence results for the data set of a non-dielectric profile plate. The convergence criteria is reached after 294 iterations in 598 seconds.

Next we test the proposed method on a data set with images of a golden colored **achromatic non-dielectric messing object** in front of a black background. This experiment will show if the method is able to identify achromatic colors. Moreover, it is investigated whether two

additional input sub-images compared to the previous data set, will improve the results. The acquired data set is given in Figure 4-11. Note, that these are images of a curved object. This implies that for the area's in the image where the surface normal does not point towards the camera, the assumptions made in the Dichromatic Reflection Model (DRM) do not hold.

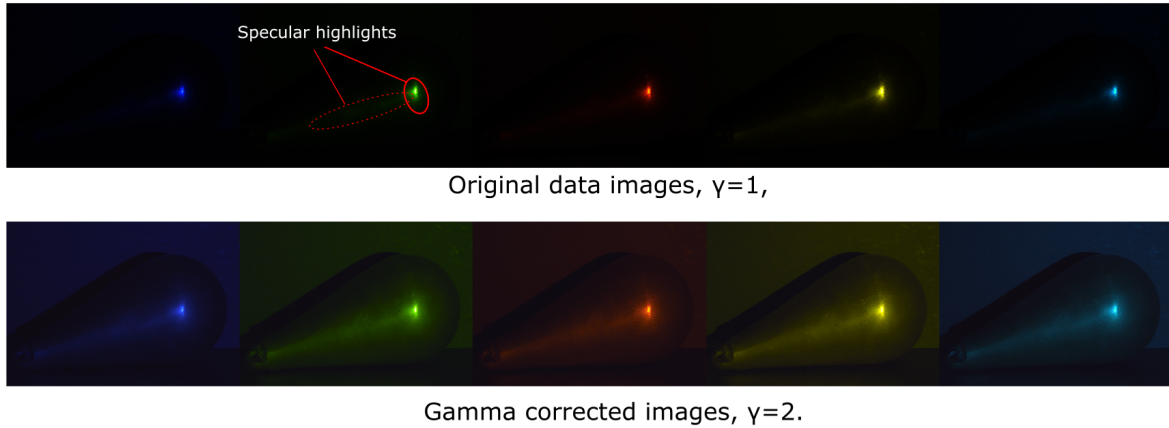


**Figure 4-11:** Acquired data images of a non-dielectric messing object. Both the original data images and gamma corrected ( $\gamma = 2$ ) data are shown and scaled for maximum contrast. A large single specular highlight can be distinguished on each of the sub-images, together with a weaker specular highlight where the surface normal of the object is in the direction of the camera.

Because there are two color regions expected in the recovered diffuse image, we set  $R = 2$ . The regularization parameters are empirically determined and set to the following values:  $\rho_s = 5$  and  $\rho_d = 2$ . Again the convergence threshold is the same,  $\epsilon = \exp(-15)$ . The results are given in Figure 4-12 and Figure 4-13.

The first thing we observe from these results is that we obtain correct localization of the specular highlights. In Figure 4-12 the specular image estimate, correctly identifies the specular reflection component and eliminates this at least partially. Again we cannot confirm the accuracy of the recovered diffuse image estimate, because there is no ground truth available. However, we can retrieve the diffuse color by using a data set with white illumination all from different directions, as described in Section 4-1-2. We find the TRUE  $W_d = [0.633, 0.646, 0.425]$ , while the estimated diffuse color of the object is equal to:  $W_d = [0.653, 0.614, 0.444]$ . This does confirm the diffuse color is accurately estimated. The recovery of the diffuse color is better compared to the data set with the aluminum profile plate, because now we have two additional input images and here the specular reflection component is more sparse compared to the other data set. The convergence plot in Figure 4-13 shows a continuous decrease in the specular regularization term, this is caused by the fact that the ratio between the specular- and diffuse regularization term is too large.

In Figure 4-14 a selection of the factorization coefficients for the reconstructed specular- and diffuse reflection components are given. We observe that at the specular highlight as the brightness increases and the color changes, the pixel values are explained as a combination of a specular- and diffuse reflection component. Especially at the peak of the specular highlight (row 410 to 420), we observe that a relatively larger fraction is explained as a specular reflection component. However, the overall ratio of specular- and diffuse coefficients is still smaller than expected for non-dielectric materials. This can be caused by the fact that the specular

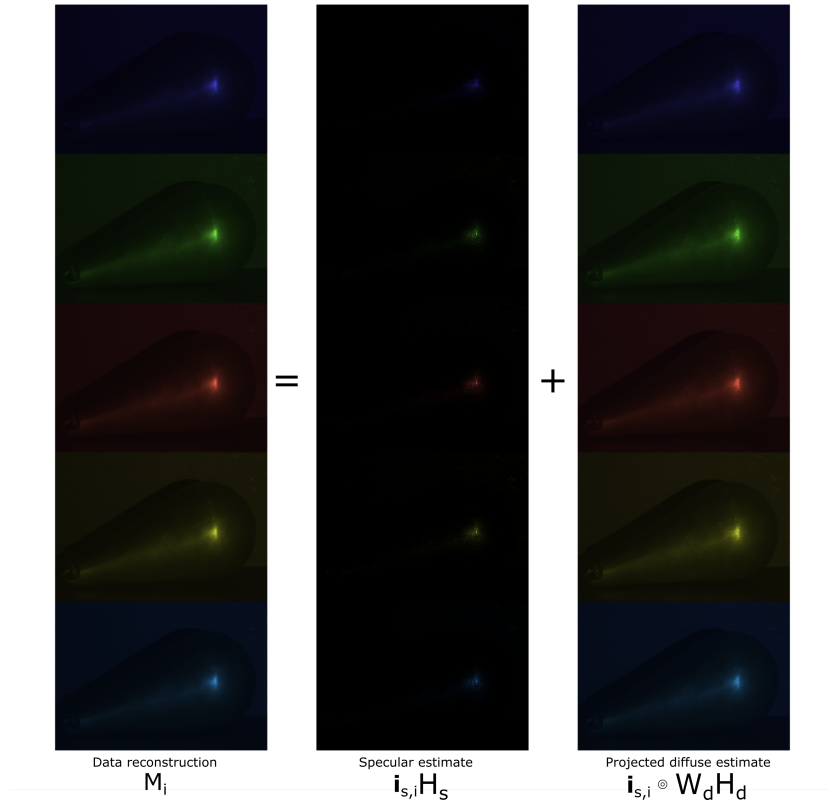


**Figure 4-12:** Results for input data images of a non-dielectric missing object, with parameters set to  $R = 2$ ,  $\rho_s = 5$  and  $\rho_d = 2$ . The data is reconstructed through the summation of a specular- and projected diffuse image estimate. The images are with gamma correction ( $\gamma = 2$ ) and scaled for maximum contrast.

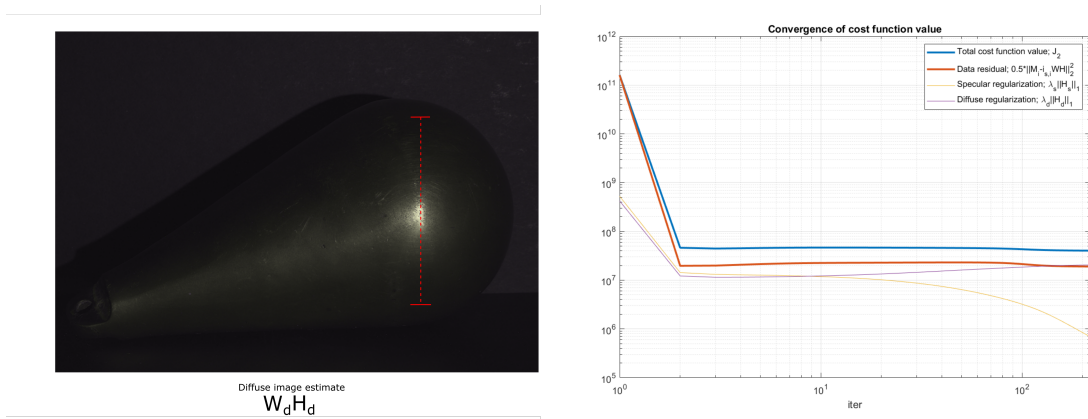


**Figure 4-13:** Left: Reconstructed diffuse image ( $W_d H_d$ ) of the non-dielectric missing object, corresponding to the results in Figure 4-12, image is with gamma correction ( $\gamma = 2$ ) and scaled for maximum contrast. The dashed red line indicates the pixels for which the specular- and diffuse coefficients are given in Figure 4-14. Right: Double logarithmic convergence results for the data set of a non-dielectric profile plate. The convergence criteria is reached after 205 iterations in 403 seconds.

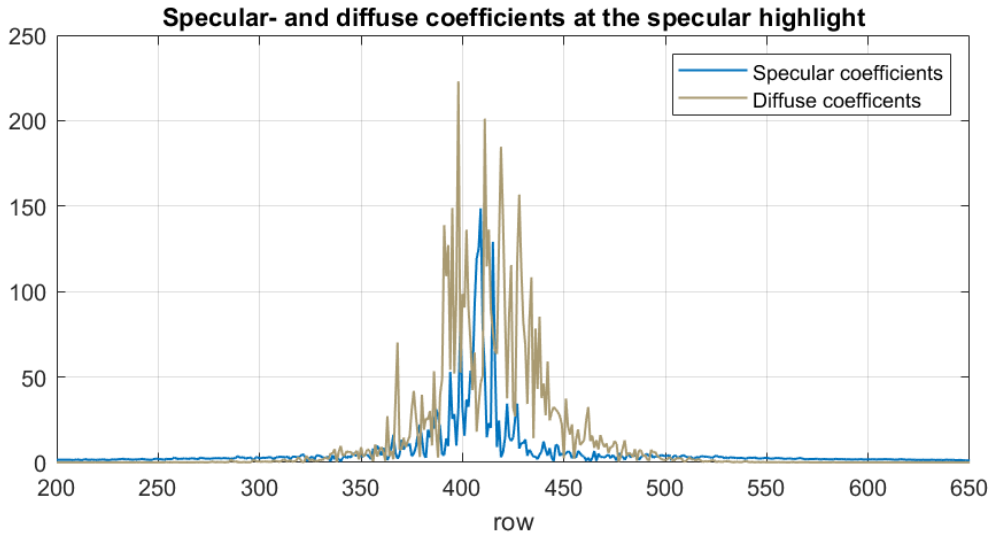


**Figure 4-14:** The reconstructed specular coefficients (from  $H_s$ ) and object color diffuse coefficients (from  $H_d$ ) for the pixels indicated by the dashed line on the left image in Figure 4-13 located at the specular highlight.

regularization parameter,  $\rho_s$ , has been set relatively high and also due to small errors in the determination of the known specular color vectors.

## 4-3 Discussion

From the results described in Section 4-2 we can make a number of general observations. The proposed multi-image optimization based specular reflection removal method is able to accurately recover the diffuse image from a synthetic data set that is generated conform the proposed reflection model. For a data set with real input images of non-dielectric objects the proposed method is able to accurately identify the locations of specular highlights. The specular reflection component is at least partially eliminated in the recovered diffuse image. The accuracy of the reconstructed image cannot be confirmed, because there is no ground truth data available. Especially with a larger number of input images with differently colored illumination, the diffuse color is estimated correctly.

The performance of the method strongly depends on the selection of the right values for the specular- and diffuse regularization parameters,  $\rho_s$  and  $\rho_d$ , respectively. Both parameters should be selected according to the noise present in the data, the sparsity of the respective reflection component and the ratio between both parameters. Additionally the diffuse regularization parameter should be selected with a larger value in order to enforce the column sparsity of the diffuse coefficients in  $H_d$ . Finding such a combination of parameters suitable for all pixels in the image has proven to be difficult, leading to sub-optimal values for the estimation of the reflection components in individual pixels.

The acquired data-sets with real images of non-dielectric objects typically have a relatively weak diffuse reflection magnitude relative to the specular reflection magnitude at the specular highlights. And because for these data sets saturation is avoided, the signal-to-noise ratio for

the diffuse reflection component is small. Additionally because there is no available ground truth data, it can not be validated to what degree the acquired data sets are conform the proposed reflection model.

---

## Chapter 5

---

# Conclusion

In this chapter the thesis is concluded. The main findings and contribution will be summarized in Section 5-1. In Section 5-2 recommendations are given for further improvements of specular reflection removal from non-dielectric materials.

### 5-1 Summary of study

Specular highlights can appear on any illuminated surface. The presence of these highlights can obscure details, like color and texture information of the surface. Certain computer vision applications that aim to identify properties of a surface from photographed images, suffer from specular highlights. Especially non-dielectric materials present large and bright specular highlights. Governed by the Fresnel equations the reflection components of these materials are particularly dependent on the imaging geometry and spectral properties.

To solve this problem a variety of specular reflection removal methods have been developed. Optimization based and color-space analysis based single-image methods have shown to be efficient and effective in the elimination of the specular reflection components from images of dielectric objects. A sparse non-negative matrix factorization of the input images, is useful in specular reflection removal methods because of its characteristic representation of the data. Single-image methods however, are not generally applicable to images with reflections from non-dielectric materials, because of the reflection properties of this material type. Multi-image methods have been successfully applied for the removal of specular reflections from non-dielectric material, however typically these method require a complex imaging setup.

A new reflection model is proposed, based on the Dichromatic Reflection Model (DRM). The model allows for colored illumination, by writing the data pixel values as a sum of specular term and a projected diffuse term. The model can be written for all pixels simultaneously as a non-negative matrix factorization. Images of the same scene but with a different illumination color, can be modeled as a projection of the specular intensity profile and diffuse image, which are identical for each image. This implies multiple images can be represented with a

significant reduction of the dimensionality of the data.

A multi-image optimization based specular reflection removal method is proposed based on the new model. The specular reflection component is eliminated by minimizing the residual between the model and data. A regularization term on the intensity coefficients is added to the cost function, such that possible noise in the data is ignored and a sparse solution is obtained. The distinction between specular- and diffuse regularization is made, such that the sparsity in the solution of the respective reflection components can be individually tuned to the data. The ill-posed bi-convex optimization problem is solved, using the alternating optimization of two constrained quadratic optimization problems.

The proposed method is evaluated by experiments on a number of data sets. A synthetic data set is generated exactly conform the proposed model, for which the ground truth of the reflection components is known. Real data sets of non-dielectric samples is acquired through the design of an imaging setup in a lab environment. The imaging setup is such that reflection components in the photographed images, closely resemble the reflection model.

The performance of the specular reflection removal method on synthetic data is evaluated by computing the Mean Squared Error (MSE) and Structural Similarity Index (SSIM) of the estimated diffuse image. The results for the synthetic data indicate that, assuming the data is indeed conform the proposed model, the diffuse image can be accurately recovered (i.e. the specular reflection component is successfully eliminated). The synthetic data set is used to test the sensitivity of the method to the specular- and diffuse regularization parameters. The result show that a good selection for these parameters is difficult to find. The optimal parameter selection depends on the noise in the data, the sparsity and magnitude of the respective specular- and diffuse reflection components, but the ratio between the two parameters also strongly affects the results.

The results of the proposed method on real images of non-dielectric objects indicate that the algorithm is able to accurately determine the intrinsic diffuse color of the object. Because there is no ground-truth available, the accuracy of the recovered diffuse image cannot be quantified. However, the results show that at the location of specular highlights, significant parts of the pixel values are explained as a specular reflection component. This allows us to conclude that the developed method is able to successfully locate and at least partially separate the specular reflection component from a small set of images of a non-dielectric object. Again the performance of the method proves sensitive to the selection of regularization parameters. Finding a good combination of parameters is especially difficult for real non-dielectric data sets, because typically the average diffuse signal is very weak compared to the intensity at the specular highlights.

## 5-2 Outlook

We can propose a number of recommendations for future improvements of the developed method and multi-image optimization based specular reflection removal from non-dielectric materials in general.

Firstly, the available information in the acquired data images may be improved by adding an ambient illumination source. This would improve the magnitude of the diffuse reflection component with respect to the noise- and specular signal. Currently this does not fit with the

formulation and assumption of the reflection model. But it should be investigated whether the model can be extended to account for (colored) ambient illumination. Additionally, we can consider acquiring data with a hyperspectral camera. Using a spectral representation of the data, the specular- and diffuse reflection components may be separated more easily according to their respective spectral distributions.

The regularization parameters are currently selected based on global properties of the input data, which leads to sub-optimal parameters for the identification of the reflection coefficients of individual pixels. This may be improved by defining two different set of regularization parameters for pixels with and without a suspected specular reflection component. Alternatively, the regularization parameter can be scaled depending on the local pixel intensities.

The Alternating Direction Method of Multipliers (ADMM) may also prove useful in efficiently solving the sparse Non-negative Matrix Factorization (NMF) optimization problem. In [6] it is stated that ADMM can be used for large-scale bi-lateral problems, and is able to deal with non-linear constraints. It should be investigated whether additional prior knowledge on specular highlights can be added as constraints within this optimization framework.



---

# Bibliography

- [1] Yasushi Akashi and Takayuki Okatani. Separation of reflection components by sparse non-negative matrix factorization. *Computer Vision and Image Understanding*, 146:77–85, May 2016.
- [2] Habibullah Akbar and Nanna Suryana Herman. Sparse coded decomposition for single image-based specular removal. In *2016 International Symposium on Electronics and Smart Devices (ISESD)*. IEEE, November 2016.
- [3] Alessandro Artusi, Francesco Banterle, and Dmitry Chetverikov. A survey of specular removal methods. *Computer Graphics Forum*, 30(8):2208–2230, August 2011.
- [4] E. F. Barkman, editor. *Appearance of Metallic Surfaces*. ASTM International, January 1970.
- [5] A. Blake and G. Brelstaff. Geometry from specularities. In *[1988 Proceedings] Second International Conference on Computer Vision*. IEEE.
- [6] Stephen Boyd. Distributed optimization and statistical learning via the alternating direction method of multipliers. *Foundations and Trends® in Machine Learning*, 3(1):1–122, 2010.
- [7] M. Claybourn, P. Colombel, and J. Chalmers. ChaRacterization of carbon-filled polymers by specular reflectance. *Applied Spectroscopy*, 45(2):279–286, February 1991.
- [8] J. Eggert and E. Korner. Sparse coding and nmf. In *2004 IEEE International Joint Conference on Neural Networks (IEEE Cat. No.04CH37541)*, volume 4, pages 2529–2533 vol.4, 2004.
- [9] Augustine Jean Fresnel. *Memoire sur la loi des modifications que la reflexion imprime a la lumiere polarisee*. De l’Imprimerie de Firmin Didot Freres, Paris, 1834.
- [10] Gang Fu, Qing Zhang, Chengfang Song, Qifeng Lin, and Chunxia Xiao. Specular highlight removal for real-world images. *Computer Graphics Forum*, 38(7):253–263, October 2019.

- [11] Jonas. Gomes, Luiz. Velho, and Mario. Costa. *Computer graphics: Theory and practice*. CRC Press LLC, 2012.
- [12] Jie Guo, Zuojian Zhou, and Limin Wang. Single image highlight removal with a sparse and low-rank reflection model. In *Computer Vision – ECCV 2018*, pages 282–298. Springer International Publishing, 2018.
- [13] Daniel Heydecker, Georg Maierhofer, Angelica I. Aviles-Rivero, Qingnan Fan, Dongdong Chen, Carola-Bibiane Schonlieb, and Sabine Susstrunk. Mirror, mirror, on the wall, who’s got the clearest image of them all?—a tailored approach to single image reflection removal. *IEEE Transactions on Image Processing*, 28(12):6185–6197, December 2019.
- [14] Patrik O. Hoyer. Non-negative matrix factorization with sparseness constraints. *J. Mach. Learn. Res.*, 5:1457–1469, December 2004.
- [15] Gudrun J. Klinker, Steven A. Shafer, and Takeo Kanade. Image segmentation and reflection analysis through color. In Mohan M. Trivedi, editor, *Applications of Artificial Intelligence VI*. SPIE, March 1988.
- [16] Gudrun J. Klinker, Steven A. Shafer, and Takeo Kanade. The measurement of highlights in color images. *International Journal of Computer Vision*, 2(1):7–32, June 1988.
- [17] Gudrun J. Klinker, Steven A. Shafer, and Takeo Kanade. A physical approach to color image understanding. *International Journal of Computer Vision*, 4(1):7–38, January 1990.
- [18] D. Lee and H. S. Seung. Learning the parts of objects by non-negative matrix factorization. *Nature*, 401:788–791, 1999.
- [19] Sang Wook Lee and Ruzena Bajcsy. Detection of specularities using colour and multiple views. *Image and Vision Computing*, 10(10):643–653, December 1992.
- [20] Ranyang Li, Junjun Pan, Yaqing Si, Bin Yan, Yong Hu, and Hong Qin. Specular reflections removal for endoscopic image sequences with adaptive-RPCA decomposition. *IEEE Transactions on Medical Imaging*, 39(2):328–340, February 2020.
- [21] Shree K. Nayar, Xi-Sheng Fang, and Terrance Boult. *International Journal of Computer Vision*, 21(3):163–186, 1997.
- [22] S.K. Nayar, X.-S. Fang, and T. Boult. Removal of specularities using color and polarization. In *Proceedings of IEEE Conference on Computer Vision and Pattern Recognition*. IEEE Comput. Soc. Press.
- [23] Edward D Palik and Gorachand Ghosh. *Handbook of Optical Constants of Solids*. Elsevier Science Technology, 1997.
- [24] Bui Tuong Phong. Illumination for computer generated pictures. *Communications of the ACM*, 18(6):311–317, June 1975.
- [25] Vítor Ramos. SIHR: a MATLAB/GNU octave toolbox for single image highlight removal. *Journal of Open Source Software*, 5(45):1822, January 2020.

- 
- [26] Yoichi Sato and Katsushi Ikeuchi. Temporal-color space analysis of reflection. *Journal of the Optical Society of America A*, 11(11):2990, November 1994.
- [27] Steven A. Shafer. *Using Color to Separate Reflection Components*, page 43–51. Jones and Bartlett Publishers, Inc., USA, 1992.
- [28] Falak Shah, Pratik Shah, and Rahul Dubey. Specularity removal for robust road detection. In *2016 IEEE Region 10 Conference (TENCON)*. IEEE, November 2016.
- [29] Syed. M. Z. Abbas Shah, Stephen Marshall, and Paul Murray. Removal of specular reflections from image sequences using feature correspondences. *Machine Vision and Applications*, 28(3-4):409–420, February 2017.
- [30] R.T. Tan and K. Ikeuchi. Separating reflection components of textured surfaces using a single image. *IEEE Transactions on Pattern Analysis and Machine Intelligence*, 27(2):178–193, February 2005.
- [31] R.T. Tan, K. Nishino, and K. Ikeuchi. Separating reflection components based on chromaticity and noise analysis. *IEEE Transactions on Pattern Analysis and Machine Intelligence*, 26(10):1373–1379, October 2004.
- [32] T.T. Tan, K. Nishino, and K. Ikeuchi. Illumination chromaticity estimation using inverse-intensity chromaticity space. In *2003 IEEE Computer Society Conference on Computer Vision and Pattern Recognition, 2003. Proceedings.* IEEE Comput. Soc.
- [33] Michael W. Tao, Jong-Chyi Su, Ting-Chun Wang, Jitendra Malik, and Ravi Ramamoorthi. Depth estimation and specular removal for glossy surfaces using point and line consistency with light-field cameras. *IEEE Transactions on Pattern Analysis and Machine Intelligence*, 38(6):1155–1169, June 2016.
- [34] Bonekamp J. W. *Literature Study on Specular Reflection Removal from Non-dielectric Surfaces*. TUDelft, Delft, March 2021.
- [35] Z. Wang, A.C. Bovik, H.R. Sheikh, and E.P. Simoncelli. Image quality assessment: From error visibility to structural similarity. *IEEE Transactions on Image Processing*, 13(4):600–612, April 2004.
- [36] L.B. Wolff. Polarization-based material classification from specular reflection. *IEEE Transactions on Pattern Analysis and Machine Intelligence*, 12(11):1059–1071, 1990.



---

# Glossary

## List of Acronyms

<b>DCSC</b>	Delft Center for Systems and Control
<b>NMF</b>	Non-negative Matrix Factorization
<b>ADMM</b>	Alternating Direction Method of Multipliers
<b>N4CI</b>	Numerics for Control and Identification
<b>DRM</b>	Dichromatic Reflection Model
<b>MSE</b>	Mean Squared Error
<b>SSIM</b>	Structural Similarity Index

## List of Symbols

$\epsilon$	Convergence threshold value
$\lambda$	Wavelength of light
$\theta_i$	Incident angle with respect to the surface normal
$\theta_r$	Specular reflection angle with respect to the surface normal
$\theta_t$	Transmittance angle with respect to the surface normal
$\rho$	Regularization parameter
$\mathbf{i}_d$	Normalized diffuse color vector
$\mathbf{i}_p$	RGB pixel value
$\mathbf{i}_s$	Normalized specular color vector
$R$	Fresnel ratio
$H$	Coefficient factorization matrix in NMF
$H_d$	Diffuse coefficient factorization matrix
$H_s$	Specular coefficient factorization matrix
$L$	Observer direction

M	Non-negative data matrix
$M_i$	Reconstruction of the $i$ 'th input image
N	Total pixel amount
R	Amount of diffuse colors
W	Basis vector factorization matrix in NMF
$W_d$	Normalized diffuse color factorization matrix